Turbulent Thermochemical Non-Equilibrium Reentry Flows with Magnetic Actuation in 2D – Eleven Species

Edisson Sávio de Góes Maciel

Rua Santa Clara, 245 – Cx. Postal: 2029 – 12.243-970 – São José dos Campos – SP – Brazil

Abstract In this work, a study involving the Maciel scheme to solve the reactive Favre averaged Navier-Stokes equations, coupled with a turbulence model and the Maxwell equations is performed. The Favre averaged Navier-Stokes equations coupled with the Maxwell equations, in conservative and finite volume contexts, employing structured spatial discretization, are studied. Eleven species chemical models, based on the works of Dunn and Kang and of Park are considered for the numerical experiments. Turbulence is taken into account considering the implementation of five k-ω two-equation turbulence models, based on the works of Coakley 1983; Wilcox; Yoder, Georgiadids and Orkwis; Coakley 1997; and Rumsey, Gatski, Ying and Bertelrud. For the magnetic coupling, the Gaitonde formulation is taken into account. The "hot gas" hypersonic flow around a blunt body is the numerical experiment for comparisons. The results have indicated that the Maciel scheme using the Dunn and Kang chemical model coupled with the Coakley 1983 turbulence model yields the best prediction of the stagnation pressure value and the best prediction of the lift coefficient. On the other hand, the Maciel scheme using the Park chemical model coupled with the Coakley 1997 turbulence model is more computationally efficient. Errors in the stagnation pressure estimation inferior to 5.00% were found.

Keywords Favre averaged Navier-Stokes and Maxwell equations, Turbulent flow, Magnetic formulation, Hypersonic flow, Reentry conditions

1. Introduction

Renewed interest in the area of hypersonic flight has brought Computational Fluid Dynamics (CFD) to the forefront of fluid flow research [1]. Many years have seen a quantum leap in advancements made in the areas of computer systems and software which utilize them for problem solving. Sophisticated and accurate numerical algorithms are devised routinely that are capable of handling complex computational problems. Experimental test facilities capable of addressing complicated high-speed flow problems are still scarce because they are too expensive to build and sophisticated measurements techniques appropriate for such problems, such as the non-intrusive laser, are still in the development stage. As a result, CFD has become a vital tool in the flow problem solution.

The study of hypersonic flows has gained momentum with the advent of concepts like the National AeroSpace Plane (NASP) and similar transatmospheric vehicles. Under the very high velocity and temperature conditions experienced by hypersonic vehicles, departure from chemical and thermal equilibrium occurs. Properties of air change dramatically as new chemical species are produced at the expense of others. The simple one temperature model used to describe the energy of air becomes inapplicable, and it becomes necessary to consider one or more additional temperatures (corresponding to vibrational and electronic energies). Determination of aerothermal loads on blunt bodies in such an environment is of great importance.

In high speed flows, any adjustment of chemical composition or thermodynamic equilibrium to a change in local environment requires certain time. This is because the redistribution of chemical species and internal energies

require certain number of molecular collisions, and hence a certain characteristic time. Chemical non-equilibrium occurs when the characteristic time for the chemical reactions to reach local equilibrium is of the same order as the characteristic time of the fluid flow. Similarly, thermal non-equilibrium occurs when the characteristic time for translation and various internal energy modes to reach local equilibrium is of the same order as the characteristic time of the fluid flow. Since chemical and thermal changes are the results of collisions between the constituent particles, non-equilibrium effects prevail in high-speed flows in low-density air.

In chemical non-equilibrium flows the mass conservation equation is applied to each of the constituent species in the gas mixture. Therefore, the overall mass conservation equation is replaced by as many species conservation equations as the number of chemical species considered. The assumption of thermal non-equilibrium introduces additional energy conservation equations – one for every additional energy mode. Thus, the number of governing equations for non-equilibrium flow is much bigger compared to those for perfect gas flow. A complete set of governing equations for non-equilibrium flow may be found in [2-3].

The problems of chemical non-equilibrium in the shock layers over vehicles flying at high speeds and high altitudes in the Earth's atmosphere have been discussed by several investigators [4-7]. Most of the existing computer codes for calculating the non-equilibrium reacting flow use the one-temperature model, which assumes that all of the internal energy modes of the gaseous species are in equilibrium with the translational mode [6-7]. It has been pointed out that such a one-temperature description of the flow leads to a substantial overestimation of the rate of equilibrium because of the elevated vibrational temperature [5]. A three-temperature chemical-kinetic model has been proposed by [8] to describe the relaxation phenomena correctly in such a flight regime. However, the model is quite complex and requires many chemical rate parameters which are not yet known. As a compromise between the three-temperature and the conventional one-temperature model, a two-temperature chemical-kinetic model has been developed [9-10], which is designated herein as the TTv model. The TTv model uses one temperature T to characterize both the translational energy of the atoms and molecules and the rotational energy of the molecules, and another temperature Tv to characterize the vibrational energy of the molecules, translational energy of the electrons, and electronic excitation energy of atoms and molecules. The model has been applied to compute the thermodynamic properties behind a normal shock wave in a flow through a constant-area duct [9-10]. Radiation emission from the non-equilibrium flow has been calculated using the Non-equilibrium Air Radiation (NEQAIR) program [11-12]. The flow and the radiation computations have been packaged into a single computer program, the Shock-Tube Radiation Program (STRAP) [10].

In spite of the advances made in the area of compressible turbulence modeling in recent years, no universal turbulence model, applicable to such complex flow problems has emerged so far. While the model should be accurate it should also be economical to use in conjunction with the governing equations of the fluid flow. Taking these issues into consideration, k-ω two-equation models have been chosen in the present work [13-17]. These models solve differential equations for the turbulent kinetic energy and the vorticity. Additional differential equations for the variances of temperature and species mass fractions have also been included. These variances have been used to model the turbulence-chemistry interactions in the reacting flows studied here.

The effects associated with the interaction of magnetic forces with conducting fluid flows have been profitably employed in several applications related to nuclear and other [18] technologies and are known to be essential in the explanation of astrophysical phenomena. In recent years, however, the study of these interactions has received fresh impetus in the effort to solve the problems of high drag and thermal loads encountered in hypersonic flight. The knowledge that electrical and magnetic forces can have profound influence on hypersonic flow fields is not new [19-20]– note increased shock-standoff and reduced heat transfer rates in hypersonic flows past blunt bodies under the application of appropriate magnetic fields. The recent interest stems, however, from new revelations of a Russian concept vehicle, known as AJAX [21], which made extensive reference to technologies requiring tight coupling between electromagnetic and fluid dynamic phenomena. A magnetogasdynamics (MGD) generator was proposed [22] to extract energy from the incoming air while simultaneously providing more benign flow to combustion components downstream. The extracted energy could then be employed to increase thrust by MGD pumping of the flow exiting the nozzle or to assist in the

generation of a plasma for injection of the body. This latter technique is known to not only reduce drag on the body but also to provide thermal protection [23].

In addition to daunting engineering challenges, some of the phenomena supporting the feasibility of an AJAX type vehicle are fraught with controversy (see, for example, [24]). Resolution of these issues will require extensive experimentation as well as simulation. The latter approach requires integration of several disciplines, including fluid dynamics, electromagnetics, chemical kinetics, and molecular physics amongst others. This paper describes a recent effort to integrate the first three of these, within the assumptions that characterize ideal and non-ideal magnetogasdynamics.

In the present work, a study involving the Maciel scheme to solve the reactive Favre averaged Navier-Stokes equations, coupled with a turbulence model and the Maxwell equations is performed. The Favre averaged Navier-Stokes equations coupled with the Maxwell equations, in conservative and finite volume contexts, employing structured spatial discretization, are studied. Turbulence is taken into account considering the implementation of five k-ω two-equation turbulence models, based on the works of [13-17]. For the magnetic formulation, the [25-26] model is implemented. The "hot gas" hypersonic flow around a blunt body, in two-dimensions, is simulated. The convergence process is accelerated to steady state condition through a spatially variable time step procedure, which has proved effective gains in terms of computational acceleration [27-28]. The reactive simulations involve Earth atmosphere chemical models of eleven species and thirty-two reactions, based on the [29] model, and eleven species and forty-three reactions, based on the [30] model. N, O, N_2, O_2, NO, N^+, O^+, N_2^+, O_2^+, NO^+ and e^- species are used to perform the numerical comparisons. The results have indicated that the Maciel scheme using the [29] chemical model coupled with the [13] turbulence model yields the best prediction of the stagnation pressure value and the best prediction of the lift coefficient. On the other hand, the Maciel scheme using the [30] chemical model coupled with the [16] turbulence model is more computationally efficient.

2. Favre Average

The Navier-Stokes equations and the equations for energy and species continuity which governs the flows with multiple species undergoing chemical reactions have been used [31, 32, 33] for the analysis. Details of the present implementation for each chemical model, the specification of the thermodynamic and transport properties, as well the vibrational model are described in [34-35]. Density-weighted averaging [36] is used to derive the turbulent flow equations from the above relations. The dependent variables, with exception of density and pressure, are written as,

$$\phi = \tilde{\phi} + \phi'', \tag{1}$$

where the ϕ'' is the fluctuating component of the variable under consideration and its Favre-mean $\tilde{\phi}$ is defined as

$$\tilde{\phi} \equiv \frac{\overline{\rho\phi}}{\overline{\rho}}. \tag{2}$$

In this equation, the overbar indicates conventional time-averaging. Density and pressure are split in the conventional sense as,

$$\rho = \overline{\rho} + \rho' \text{ and } p = \overline{p} + p'. \tag{3}$$

The average continuity and momentum equations are

$$\frac{\partial\overline{\rho}}{\partial t} + \frac{\partial\overline{\rho}\tilde{U}_i}{\partial x_i} = 0 \, ; \tag{4}$$

$$\frac{\partial\overline{\rho}\tilde{U}_i}{\partial t} + \frac{\partial\overline{\rho}\tilde{U}_i\tilde{U}_j}{\partial x_j} = -\frac{\partial\overline{p}}{\partial x_i} - \frac{\partial\overline{\rho u_i'' u_j''}}{\partial x_j} + \frac{\partial\overline{\tau_{ij}}}{\partial x_j} , \tag{5}$$

where:

$$\tau_{ij} = \mu\left(\frac{\partial u_i}{\partial x_j} + \frac{\partial u_j}{\partial x_i}\right) - \frac{2}{3}\frac{\partial u_k}{\partial x_k}\delta_{ij} \tag{6}$$

with repeated indices indicating summation. The mass-averaged total energy can be written in terms of the total enthalpy as

$$\frac{\tilde{e}}{\overline{\rho}} = \tilde{H} - \frac{\overline{p}}{\overline{\rho}} \; . \tag{7}$$

Using the above definition and omitting the body force contribution, the time-averaged energy equation is

$$\frac{\partial \tilde{e}}{\partial t} + \frac{\partial (\tilde{e} + \overline{p})\tilde{U}_j}{\partial x_j} = -\frac{\partial \overline{q_j}}{\partial x_j} + \frac{\partial \overline{u_i \tau_{ij}}}{\partial x_j} - \frac{\partial \overline{\rho u_j'' H''}}{\partial x_j} \; , \tag{8}$$

where $\overline{q_j}$ represents the averaged heat flux term. The species conservation equation is

$$\frac{\partial \overline{\rho}\tilde{c}_i}{\partial t} + \frac{\partial \overline{\rho}\tilde{c}_i \tilde{U}_j}{\partial x_j} = \overline{\dot{\omega}}_i - \frac{\partial\left(\overline{\rho u_j'' c_i''} + \overline{\rho c_i (V_i)_j}\right)}{\partial x_j} \; . \tag{9}$$

The equations for the two turbulence variables, turbulent kinetic energy (k) and vorticity (ω), are derived using the momentum and continuity equations and time-averaging procedure [37-38]. These equations are presented in the fourth section.

3. Modeled Equations

Closure of the averaged equations is achieved by invoking the Boussinesq approximation in which relates the turbulent stresses (Reynolds stresses) to the mean strain rate. The Reynolds stress tensor is written as,

$$-\overline{\rho u_i'' u_j''} = \overline{\mu}_T S_{ij} - \frac{2}{3}\overline{\rho}k\delta_{ij}, \text{ where: } S_{ij} = \frac{\partial \tilde{U}_i}{\partial x_j} + \frac{\partial \tilde{U}_j}{\partial x_i} - \frac{2}{3}\frac{\partial \tilde{U}_k}{\partial x_k}\delta_{ij} \tag{10}$$

in which μ_T is the turbulent/eddy viscosity and its definition depends of the construction of the studied k-ω model.

The correlation between fluctuating velocity and the scalar fluctuations are modeled in a similar manner using a mean gradient hypothesis. A typical model is,

$$-\overline{\rho u_i'' \phi''} = \frac{\overline{\mu}_T}{\sigma_\phi}\left(\frac{\partial \tilde{\phi}}{\partial x_i}\right), \tag{11}$$

where σ_ϕ is a coefficient which, normally, is a constant. For $\phi = c_i$, $\sigma_\phi = Sc_T$ (turbulent Schmidt number) and for the static enthalpy, $\phi = h$, $\sigma_\phi = Prd_T$ (turbulent Prandtl number).

The mean continuity equation, Eq. (4), does not require any further modeling. The modeled momentum equation is,

$$\frac{\partial \overline{\rho}\tilde{U}_i}{\partial t} + \frac{\partial \overline{\rho}\tilde{U}_i \tilde{U}_j}{\partial x_j} = -\frac{\partial \overline{p}}{\partial x_i} + \frac{2}{3}\frac{\partial \overline{\rho}k}{\partial x_j}\delta_{ij} - \frac{\partial\left[(\overline{\mu} + \overline{\mu}_T)S_{ij}\right]}{\partial x_j} \; . \tag{12}$$

The correlation $\overline{\rho u_j'' H''}$ in the thermodynamic energy equation, Eq. (8), is split into its components as

$$\overline{\rho u_j'' H''} = \overline{\rho u_j'' h''} + \frac{\overline{\rho u_i'' u_i'' u_j''}}{2} + \overline{\rho u_i'' u_j''}\tilde{U}_i \; . \tag{13}$$

The modeled energy equation then is,

$$\frac{\partial \tilde{e}}{\partial t} + \frac{\partial (\tilde{e} + \bar{p}) \tilde{U}_j}{\partial x_j} = \frac{\partial \left(\overline{\tau_{ij} - \rho u_i'' u_j''} \right) \tilde{U}_i}{\partial x_j} + \frac{\partial}{\partial x_j} \left[\left(\frac{\bar{\mu}}{Pr d_L} + \frac{\bar{\mu}_T}{Pr d_T} \right) \frac{\partial \tilde{h}}{\partial x_j} + \left(\bar{\mu} + \frac{\bar{\mu}_T}{\sigma_k} \right) \frac{\partial k}{\partial x_j} \right],$$ (14)

Where σ_k is a coefficient that appears in the turbulent kinetic energy equation. The modeled species continuity equation is

$$\frac{\partial \bar{\rho} \tilde{c}_i}{\partial t} + \frac{\partial \bar{\rho} \tilde{c}_i \tilde{U}_j}{\partial x_j} = \bar{\dot{\omega}}_i - \frac{\partial}{\partial x_j} \left[\left(\frac{\bar{\mu}}{Sc} + \frac{\bar{\mu}_T}{Sc_T} \right) \frac{\partial \tilde{c}_i}{\partial x_j} \right].$$ (15)

Differential equations for the variances of static enthalpy and species mass fractions have also been introduced in the solutions. Equations for $\overline{h'' h''}$ and $\overline{c_i'' c_i''}$ have been derived. The modeled equations take a similar form as that of the turbulent kinetic energy (to be seen in the next section). These equations are given below.

$$\frac{\partial \bar{\rho} g}{\partial t} + \frac{\partial \bar{\rho} g \tilde{U}_j}{\partial x_j} = -2 \overline{\rho u_j'' G''} \frac{\partial \tilde{G}}{\partial x_j} + \frac{\partial}{\partial x_j} \left[\left(\frac{\bar{\mu}}{\sigma} + \frac{\bar{\mu}_T}{\sigma_g} \right) \frac{\partial g}{\partial x_j} \right] + \Psi,$$ (16)

where for $g = \overline{h'' h''}$, $G = \tilde{h}$, $\Psi = 0$, $\sigma = Pr d_L$(laminar Prandtl number) and $\sigma_g = Pr d_T$ and for $g = \sum_{i=1}^{ns} \overline{c_i'' c_i''}$, $G = \sum_{i=1}^{ns} \tilde{c}_i$, $\Psi = 2 \sum_{i=1}^{ns} \overline{\dot{\omega}_i c_i''}$, $\sigma = Sc$ and $\sigma_g = Sc_T$, with "ns" being the total number of species.

The g-equations for the species variances are summed over all species to obtain an equation for the turbulent scalar energy (Q_s) defined as

$$Q_s = \sum_{i=1}^{ns} \overline{c_i'' c_i''}$$ (17)

and this equation is solved instead of the individual species variance equations. The production term [first term on the right hand side of Eq. (16)] is evaluated using Eq. (11).

In a system involving J reaction steps and N species, the instantaneous production rate of a scalar i can be represented – from the law of mass action – in the following most general form:

$$\dot{\omega}_i = M_i \sum_{j=1}^{J} \left(v_{ij}'' - v_{ij}' \right) \left\{ k_{fj} \rho^{m_j} \prod_{i=1}^{N} \left(\frac{c_i}{M_i} \right)^{v_{ij}'} - k_{bj} \rho^{n_j} \prod_{i=1}^{N} \left(\frac{c_i}{M_i} \right)^{v_{ij}''} \right\},$$ (18)

Where $m_j = \sum_{i=1}^{N} v_{ij}'$ and $n_j = \sum_{i=1}^{N} v_{ij}''$. In the above equations, the number of molecules of the scalar i involved in the j-th forward reaction is v_{ij}' and in the corresponding backward reaction is v_{ij}''. The forward and backward rate-constants of the reaction j are given by k_{fj} and k_{bj}, respectively. Typically the reaction rates are functions of the temperature:

$$k_{fj} = A_j T^{b_j} \exp \left[-\frac{T_{aj}}{T} \right],$$ (19)

Where A_j, b_j, and T_{aj} are numerical constants specific to the given reaction.

The purpose of solving the g-equations is to include the interaction between turbulence and chemical reactions in the reacting flow cases. The effect of temperature fluctuations on the species production rate is included using an approximate analysis. Here, the Arrhenius equations for the reaction rate term are written in terms of mean and fluctuating components of the temperature and expanded in the form of a series. The terms are truncated at the second order level of the fluctuations and the calculated variance of temperature is used to evaluate the resultant reaction rate term. The reaction rate term is given by the Arrhenius rate equation [Eq. (19)].

$$k_f = AT^b \exp\left[-\frac{T_a}{T}\right]. \tag{20}$$

Using Eq. (1), this can be written as

$$k_f = A(\widetilde{T} + T'')T^b \exp\left[-\frac{T_a}{(\widetilde{T} + T'')}\right]. \tag{21}$$

Assuming that $\dfrac{T''}{\widetilde{T}} < 1$, the term $(\widetilde{T} + T'')$ can be expanded in a series and the resultant modified reaction rate term is (in a Favre averaged form),

$$k_f = (1+m)A\widetilde{T}^b \exp\left[-\frac{T_a}{\widetilde{T}}\right], \tag{22}$$

where:

$$m = \left[(b-1)\left(\frac{b}{2}+\frac{T_a}{\widetilde{T}}\right)+\frac{1}{2}\left(\frac{T_a}{\widetilde{T}}\right)^2\right]\frac{\overline{T''T''}}{\widetilde{T}^2}. \tag{23}$$

In the above, T_a is the activation temperature and A is the pre-exponential factor in the Arrhenius equation. Terms of order higher than two in $\dfrac{T''}{\widetilde{T}}$ are neglected from the series expansion in the present analysis. The factor m represents the effect of turbulent fluctuations in temperature on reaction rate. The maximum value of m for a temperature fluctuation of 30% mean temperature is approximately 0.6 and this is the value adopted in this work.

Practical reactive flows involve multiple scalar mixing and reactions. For such flows, [39] suggests the use of a multivariate β-pdf model to account for the effects of the scalar fluctuations on the species production rates. This model is briefly outlined below. The multivariate β-pdf for the N-scalar mixing process is given by

$$F(f) = \frac{\Gamma(\beta_1 + ... + \beta_N)}{\Gamma(\beta_1)..\Gamma(\beta_N)} f_1^{\beta_1-1} f_2^{\beta_2-1} ... f_N^{\beta_N-1} \delta(1 - f_1 - f_2 ... - f_N). \tag{24}$$

The parameters of the model $(\beta_1,...,\beta_N)$ are functions of the mean mass fractions $\widetilde{c}_i$ and turbulent scalar energy Q_s [Eq. (17)]:

$$\beta_i = \widetilde{c}_i\left(\frac{1-S}{Q_s}-1\right), \tag{25}$$

where S is given by

$$S = \sum_{i=1}^{N} \widetilde{c}_i^{\,2}. \tag{26}$$

Subject to the above simplifications the mean species production rate is given by,

$$\dot{\omega}_i = M_i \sum_{j=1}^{J} \left(v_{ij}'' - v_{ij}'\right)\left\{\overline{k_{fj}}\rho^{m_j}\left[\prod_{i=1}^{N}(M_i)^{-v_{ij}'}\right]I_{fj} - \overline{k_{bj}}\rho^{n_j}\left[\prod_{i=1}^{N}(M_i)^{-v_{ij}''}\right]I_{bj}\right\}, \tag{27}$$

in which:

$$I_{fj} \equiv \prod_{i=1}^{N} c_i^{v_{ij}'} \text{ and } I_{bj} \equiv \prod_{i=1}^{N} c_i^{v_{ij}''}. \tag{28}$$

In the above equations, angular brackets represent conventional time averaging. The expression for I_{fj} is obtained from [39],

$$I_{fj} \equiv \prod_{i=1}^{N} \prod_{r=1}^{v_{ij}'} \left(\beta_i + v_{ij}' - r\right) \Big/ \prod_{p=1}^{m_j} \left(B + m_j - p\right). \tag{29}$$

Similarly, the expression for I_{bj} is,

$$I_{bj} \equiv \prod_{i=1}^{N} \prod_{r=1}^{v_{ij}''} \left(\beta_i + v_{ij}'' - r\right) \Big/ \prod_{p=1}^{n_j} \left(B + n_j - p\right), \tag{30}$$

in which

$$B = \beta_1 + \beta_2 + ... + \beta_N. \tag{31}$$

The expression for the source term in the scalar variance (Q_s) is given by [39],

$$\sum_{i=1}^{N} \overline{\dot{\omega}_i c_i} = \sum_{i=1}^{N} M_i \sum_{j=1}^{J} \left(v_{ij}'' - v_{ij}'\right) \left\{ \overline{k_{fj}} \rho^{m_j} \left[\prod_{i=1}^{N} \left(M_i\right)^{-v_{ij}'}\right] J_{fj} - \overline{k_{bj}} \rho^{n_j} \left[\prod_{i=1}^{N} \left(M_i\right)^{-v_{ij}''}\right] J_{bj} \right\} \tag{32}$$

with

$$J_{fj} \equiv c_i \prod_{i=1}^{N} c_i^{v_{ij}'} \quad \text{and} \quad J_{bj} \equiv c_i \prod_{i=1}^{N} c_i^{v_{ij}''}. \tag{33}$$

The terms J_{fj} and J_{bj} are also moments of the scalar joint-pdf, and can be easily evaluated as

$$J_{fj} \equiv I_{fj} \frac{\beta_i + v_{ij}'}{B + m_j} \quad \text{and} \quad J_{bj} \equiv I_{bj} \frac{\beta_i + v_{ij}''}{B + n_j}. \tag{34}$$

Substitution of Eq. (34) into Eq. (32) leads to the model for the source/sink of turbulent scalar energy.

4. Favre-Averaged Navier-Stokes Equations Coupled with Maxwell Equations

The flow is modeled by the Favre-averaged Navier-Stokes equations coupled with the Maxwell equations and the condition of thermochemical non-equilibrium, where the rotational and vibrational contributions are considered, is taken into account. Details of the eleven species model implementation are described in [34-35], and the interested reader is encouraged to read these works to become aware of the present study. The reactive Navier-Stokes equations in thermal and chemical non-equilibrium were implemented on conservative and finite volume contexts, in the two-dimensional space. In this case, these equations in integral and conservative forms can be expressed by:

$$\frac{\partial}{\partial t} \int_V Q dV + \int_S \vec{F} \bullet \vec{n} dS = \int_V S_{CV} dV + \int_V G dV, \text{ with: } \vec{F} = \left(E_e - E_v\right)\vec{i} + \left(F_e - F_v\right)\vec{j}, \tag{35}$$

where: Q is the vector of conserved variables, V is the volume of a computational cell, $\vec{F}$ is the complete flux vector, $\vec{n}$ is the unity vector normal to the flux face, S is the flux area, G is the k-ω two-equation model source term, S_{CV} is the chemical and vibrational source term, E_e and F_e are the convective flux vectors or the Euler flux vectors in the x and y directions, respectively, and E_v and F_v are the viscous flux vectors in the x and y directions, respectively. The $\vec{i}$ and $\vec{j}$ unity vectors define the Cartesian coordinate system. Twenty-one (21) conservation equations are solved: one of general mass conservation, two of linear momentum conservation, one of total energy, ten of species mass conservation, one of the vibrational internal energy of the molecules, two of the k-ω turbulence model, two of the g-equations, and two of the Maxwell equations. Therefore, one of the species is absent of the iterative process. The CFD literature recommends that the species of biggest mass fraction of the gaseous mixture should be omitted, aiming to result in a minor numerical accumulation error. To the present study, in which is chosen chemical models to the air composed of eleven (11) chemical species (N, O, N_2, O_2, NO, N^+, O^+, N_2^+, O_2^+, NO^+ and e^-) and thirty-two chemical reactions to the [29] model or forty-three chemical reactions to the [30] model, this species can be the N_2 or the O_2. To this work, the N_2 was chosen. The vectors Q, E_e, F_e, E_v, F_v, G and S_{CV} can, hence, be defined as follows:

$$
Q = \left\{ \begin{array}{c} \rho \\ \rho u \\ \rho v \\ \rho Z \\ \rho_1 \\ \rho_2 \\ \rho_4 \\ \rho_5 \\ \rho_6 \\ \rho_7 \\ \rho_8 \\ \rho_9 \\ \rho_{10} \\ \rho_{11} \\ \rho e_V \\ \rho k \\ \rho \omega \\ \rho Q_h \\ \rho Q_s \\ B_x \\ B_y \end{array} \right\},\
E_e = \left\{ \begin{array}{c} \rho u \\ \rho u^2 + P - R_b\,B_x^2/\mu_M \\ \rho uv - R_b\,B_x B_y/\mu_M \\ (\rho Z + P)u - R_b\big(\vec{V} \bullet \vec{B}/\mu_M\big)B_x \\ \rho_1 u \\ \rho_2 u \\ \rho_4 u \\ \rho_5 u \\ \rho_6 u \\ \rho_7 u \\ \rho_8 u \\ \rho_9 u \\ \rho_{10} u \\ \rho_{11} u \\ \rho e_V u \\ \rho k u \\ \rho \omega u \\ \rho Q_h u \\ \rho Q_s u \\ 0 \\ uB_y - vB_x \end{array} \right\},\
F_e = \left\{ \begin{array}{c} \rho v \\ \rho uv - R_b\,B_x B_y/\mu_M \\ \rho v^2 + P - R_b\,B_y^2/\mu_M \\ (\rho Z + P)v - R_b\big(\vec{V} \bullet \vec{B}/\mu_M\big)B_y \\ \rho_1 v \\ \rho_2 v \\ \rho_4 v \\ \rho_5 v \\ \rho_6 v \\ \rho_7 v \\ \rho_8 v \\ \rho_9 v \\ \rho_{10} v \\ \rho_{11} v \\ \rho e_V v \\ \rho k v \\ \rho \omega v \\ \rho Q_h v \\ \rho Q_s v \\ vB_x - uB_y \\ 0 \end{array} \right\};\qquad (36)
$$

in which: ρ is the mixture density; u and v are Cartesian components of the velocity vector in the x and y directions, respectively; $\vec{V}$ is the complete flow velocity vector; P is the pressure term considering the magnetic effect; Z is the fluid total energy considering the contribution of the magnetic field;

$$
E_v = \left\{ \begin{array}{c} 0 \\ (t_{xx} + \tau_{xx})/Re \\ (t_{xy} + \tau_{xy})/Re \\ (f_x - \phi_x)/Re - q_{J,x}/Re_\sigma \\ (-\rho_1 v_{1x} - \theta_{1x})/Re \\ (-\rho_2 v_{2x} - \theta_{2x})/Re \\ (-\rho_4 v_{4x} - \theta_{4x})/Re \\ (-\rho_5 v_{5x} - \theta_{5x})/Re \\ (-\rho_6 v_{6x} - \theta_{6x})/Re \\ (-\rho_7 v_{7x} - \theta_{7x})/Re \\ (-\rho_8 v_{8x} - \theta_{8x})/Re \\ (-\rho_9 v_{9x} - \theta_{9x})/Re \\ (-\rho_{10} v_{10x} - \theta_{10x})/Re \\ (-\rho_{11} v_{11x} - \theta_{11x})/Re \\ (q_{v,x} - \phi_{v,x})/Re \\ \alpha_x/Re \\ \beta_x/Re \\ \gamma_x/Re \\ \delta_x/Re \\ 0 \\ \dfrac{1}{Re_\sigma}\dfrac{1}{\sigma}\left[\dfrac{\partial}{\partial x}\left(\dfrac{B_y}{\mu_M}\right) - \dfrac{\partial}{\partial y}\left(\dfrac{B_x}{\mu_M}\right)\right] \end{array} \right\},\
F_v = \left\{ \begin{array}{c} 0 \\ (t_{xy} + \tau_{xy})/Re \\ (t_{yy} + \tau_{yy})/Re \\ (f_y - \varphi_y)/Re - q_{J,y}/Re_\sigma \\ (-\rho_1 v_{1y} - \theta_{1y})/Re \\ (-\rho_2 v_{2y} - \theta_{2y})/Re \\ (-\rho_4 v_{4y} - \theta_{4y})/Re \\ (-\rho_5 v_{5y} - \theta_{5y})/Re \\ (-\rho_6 v_{6y} - \theta_{6y})/Re \\ (-\rho_7 v_{7y} - \theta_{7y})/Re \\ (-\rho_8 v_{8y} - \theta_{8y})/Re \\ (-\rho_9 v_{9y} - \theta_{9y})/Re \\ (-\rho_{10} v_{10y} - \theta_{10y})/Re \\ (-\rho_{11} v_{11y} - \theta_{11y})/Re \\ (q_{v,y} - \varphi_{v,y})/Re \\ \alpha_y/Re \\ \beta_y/Re \\ \gamma_y/Re \\ \delta_y/Re \\ \dfrac{1}{Re_\sigma}\dfrac{1}{\sigma}\left[\dfrac{\partial}{\partial y}\left(\dfrac{B_x}{\mu_M}\right) - \dfrac{\partial}{\partial x}\left(\dfrac{B_y}{\mu_M}\right)\right] \\ 0 \end{array} \right\};\qquad (37)
$$

$\vec{B}$ is the complete magnetic field vector; R_b is the magnetic force number or the pressure number; ρ_1, ρ_2, ρ_4, ρ_5, ρ_6, ρ_7, ρ_8, ρ_9, ρ_{10}, and ρ_{11} are densities of the N, O, O_2, NO, N^+, O^+, N_2^+, O_2^+, NO^+, and e^-, respectively; k is the turbulent kinetic energy; ω is the turbulent vorticity; Q_h is the product of fluctuating enthalpy, $\overline{h''h''}$; Q_s is the sum of the product of fluctuating mass fraction, $\sum_{i=1}^{ns}\overline{c_i''c_i''}$;B_x and B_y are Cartesian components of the magnetic field vector in the x and y directions, respectively; μ_M is the mean magnetic permeability, with the value of $4\pi \times 10^{-7}$T·m/A; e_V is the sum of the vibrational energy of the molecules; the τ's are the components of the Reynolds stress tensor; the t's are the components of the viscous stress tensor; f_x and f_y are viscous work and Fourier heat flux functions;$\rho_s v_{sx}$ and $\rho_s v_{sy}$ represent the species diffusion flux, defined by the Fick law; ϕ_x and ϕ_y are the terms of mixture diffusion; $\phi_{v,x}$ and $\phi_{v,y}$ are the terms of molecular diffusion calculated at the vibrational temperature; α_x, α_y, β_x, β_y, γ_x, γ_y, δ_x and δ_y are two-equation turbulence model parameters; θ_{sx} and θ_{sy} are diffusion terms function of the mass fraction gradients; $\dot{\omega}_s$ is the chemical source term of each species equation, defined by the law of mass action;e_v^* is the molecular-vibrational-internal energy calculated with the translational/rotational temperature; τ_s is the translational-vibrational characteristic relaxation time of each molecule;

$$
S_{CV} = \begin{Bmatrix} 0 \\ 0 \\ 0 \\ 0 \\ \dot{\omega}_1 \\ \dot{\omega}_2 \\ \dot{\omega}_4 \\ \dot{\omega}_5 \\ \dot{\omega}_6 \\ \dot{\omega}_7 \\ \dot{\omega}_8 \\ \dot{\omega}_9 \\ \dot{\omega}_{10} \\ \dot{\omega}_{11} \\ \sum_{s=mol}\rho_s\left(e_{v,s}^*-e_{v,s}\right)/\tau_s + \sum_{s=mol}\dot{\omega}_s e_{v,s} \\ 0 \\ 0 \\ 0 \\ 0 \\ 0 \\ 0 \end{Bmatrix} ; \quad
G = \begin{Bmatrix} 0 \\ 0 \\ 0 \\ 0 \\ 0 \\ 0 \\ 0 \\ 0 \\ 0 \\ 0 \\ 0 \\ 0 \\ 0 \\ 0 \\ 0 \\ G_k \\ G_\omega \\ \left(\dfrac{2\mu_T}{\mathrm{Re}\,\mathrm{Pr}\,d_T}\right)\left[\left(\dfrac{\partial h}{\partial x}\right)^2+\left(\dfrac{\partial h}{\partial y}\right)^2\right] \\ \left(\dfrac{2\mu_T}{\mathrm{Re}\,\mathrm{Sc}_T}\right)\left[\left(\dfrac{\partial c_T}{\partial x}\right)^2+\left(\dfrac{\partial c_T}{\partial y}\right)^2\right]+\dfrac{\Psi}{\mathrm{Re}} \\ 0 \\ 0 \end{Bmatrix} ; \quad (38)
$$

$q_{v,x}$ and $q_{v,y}$ are the vibrational Fourier heat flux components in the x and y directions, respectively; Re is the laminar Reynolds number; $q_{J,x}$ and $q_{J,y}$ are the components of the Joule heat flux vector in the x and y directions, respectively; Re_σ is the magnetic Reynolds number; σ is the electrical conductivity; G_k and G_ω are k-ω source terms; μ_T is the turbulent viscosity or vorticity viscosity; h is the static enthalpy; and c_T is the total mass fraction sum.

The viscous stresses, in N/m^2, are determined, according to a Newtonian fluid model, by:

$$t_{xx} = [2\mu_m \, \partial u/\partial x - 2/3\mu_m (\partial u/\partial x + \partial v/\partial y)] \; ;$$

$$t_{xy} = \mu_m (\partial u/\partial y + \partial v/\partial x); \tag{39a}$$

$$t_{yy} = [2\mu_m (\partial v/\partial y) - 2/3\mu_m (\partial u/\partial x + \partial v/\partial y)], \tag{39b}$$

where μ_m is the molecular viscosity. The components of the turbulent stress tensor (Reynolds stress tensor) are described by the following expressions:

$$\tau_{xx} = [2\mu_T \, \partial u/\partial x - 2/3\mu_T (\partial u/\partial x + \partial v/\partial y)] - 2/3 \mathrm{Re}\rho k \; ;$$

$$\tau_{xy} = \mu_T (\partial u/\partial y + \partial v/\partial x); \tag{40}$$

$$\tau_{yy} = [2\mu_T \, \partial v/\partial y - 2/3\mu_T (\partial u/\partial x + \partial v/\partial y)] - 2/3 \mathrm{Re}\rho k \; .$$

Expressions to f_x and f_y are given below:

$$f_x = (t_{xx} + \tau_{xx})u + (t_{xy} + \tau_{xy})v + q_x + q_{v,x} + k_x \; ; \tag{41}$$

$$f_y = (t_{xy} + \tau_{xy})u + (t_{yy} + \tau_{yy})v + q_y + q_{v,y} + k_y \, , \tag{42}$$

where q_x and q_y are the Fourier heat flux components and are given by:

$$q_x = (\mu_m/\mathrm{Prd}_L + \mu_T/\mathrm{Prd}_T)\partial h/\partial x \; ; \tag{43}$$

$$q_y = (\mu_m/\mathrm{Prd}_L + \mu_T/\mathrm{Prd}_T)\partial h/\partial y \, . \tag{44}$$

The $q_{v,x}$ and $q_{v,y}$ are the vibrational heat flux components and are given by:

$$q_{v,x} = k_V \, \partial T_V/\partial x \; ; \tag{45}$$

$$q_{v,y} = k_V \, \partial T_V/\partial y \, , \tag{46}$$

with k_V being the vibrational thermal conductivity and T_V is the vibrational temperature, what characterizes this model as of two temperatures: translational/rotational and vibrational. The last terms in Eqs. (41)-(42) are k_x and k_y and are defined as follows:

$$k_x = \left(\mu_m + \frac{\mu_T}{\sigma_k}\right)\partial k/\partial x \; ; \text{and } k_y = \left(\mu_m + \frac{\mu_T}{\sigma_k}\right)\partial k/\partial y \, . \tag{47}$$

The diffusion terms related to the k-ω equations are defined as:

$$\alpha_x = (\mu_m + \mu_T/\sigma_k)\partial k/\partial x, \; \alpha_y = (\mu_m + \mu_T/\sigma_k)\partial k/\partial y \; ; \tag{48}$$

$$\beta_x = (\mu_m + \mu_T/\sigma_\omega)\partial\omega/\partial x, \; \beta_y = (\mu_m + \mu_T/\sigma_\omega)\partial\omega/\partial y \; ; \tag{49}$$

$$\gamma_x = (\mu_m/\mathrm{Prd}_L + \mu_T/\mathrm{Prd}_T)\partial Q_h/\partial x, \; \gamma_y = (\mu_m/\mathrm{Prd}_L + \mu_T/\mathrm{Prd}_T)\partial Q_h/\partial y \; ; \tag{50}$$

$$\delta_x = (\mu_m/\mathrm{Sc} + \mu_T/\mathrm{Sc}_T)\partial Q_S/\partial x, \; \delta_y = (\mu_m/\mathrm{Sc} + \mu_T/\mathrm{Sc}_T)\partial Q_S/\partial y \, , \tag{51}$$

where the Schmidt numbers are: $\mathrm{Sc} = 0.22$ (laminar) and $\mathrm{Sc}_T = 1.00$ (turbulent). The terms of species diffusion, defined by the Fick law, to a condition of thermal non-equilibrium, are determined by [40]:

$$\rho_s v_{sx} = -\rho D_s \frac{\partial Y_{MF,s}}{\partial x} \text{ and } \rho_s v_{sy} = -\rho D_s \frac{\partial Y_{MF,s}}{\partial y} \, , \tag{52}$$

with "s" referent to a given species, $Y_{MF,s}$ being the molar fraction of the species, defined as:

$$Y_{MF,s} = \frac{\rho_s/M_s}{\sum\limits_{k=1}^{ns} \rho_k/M_k} \tag{53}$$

and D_s is the species-effective-diffusion coefficient.

The diffusion terms ϕ_x and ϕ_y which appear in the energy equation are defined by [41]:

$$\phi_x = \sum_{s=1}^{ns} \rho_s v_{sx} h_s \text{ and } \phi_y = \sum_{s=1}^{ns} \rho_s v_{sy} h_s , \tag{54}$$

being h_s the specific enthalpy (sensible) of the chemical species "s". The molecular diffusion terms calculated at the vibrational temperature, $\phi_{v,x}$ and $\phi_{v,y}$, which appear in the vibrational-internal-energy equation are defined by [40]:

$$\phi_{v,x} = \sum_{s=mol} \rho_s v_{sx} h_{v,s} \text{ and } \phi_{v,y} = \sum_{s=mol} \rho_s v_{sy} h_{v,s} , \tag{55}$$

with $h_{v,s}$ being the specific enthalpy (sensible) of the chemical species "s" calculated at the vibrational temperature T_V. The sum of Eq. (55), as also those present in Eq. (38), considers only the molecules of the system, namely: N_2, O_2, NO, N_2^+, O_2^+, and NO^+. The θ's terms of Eq. (37) are described as,

$$\theta_{sx} = \left(\mu_m/Sc + \mu_T/Sc_T\right)\partial c_S/\partial x ; \tag{56}$$

$$\theta_{sy} = \left(\mu_m/Sc + \mu_T/Sc_T\right)\partial c_S/\partial y . \tag{57}$$

The Z total energy is defined as:

$$Z = c_{v,mix}\left(T - T_{REF}\right) + \Delta h_{f,mix}^0 + e_V + 0.5\left(u^2 + v^2\right) + R_b \frac{B^2}{2\rho\mu_M} , \tag{58}$$

with: T_{REF} is the reference temperature, and $\Delta h_{f,mix}^0$ is the mixture formation enthalpy. The pressure term is expressed by:

$$P = p + R_b \frac{B_x^2 + B_y^2}{2\mu_M} = p + R_b \frac{B^2}{2\mu_M} , \tag{59}$$

with p the fluid static pressure. The magnetic force number or pressure number is determined by:

$$R_b = \frac{B_{initial}^2}{\rho_{char} V_{initial}^2 \mu_{M,char}} = \frac{B_{x,initial}^2 + B_{y,initial}^2}{\rho_{char}\left(u_{initial}^2 + v_{initial}^2\right)\mu_{M,char}} , \tag{60}$$

where $B_{initial}$, $B_{x,initial}$, $B_{y,initial}$, $V_{initial}$, $u_{initial}$ and $v_{initial}$ are initial values of the magnetic field and of the fluid flow, and ρ_{char}, $\mu_{M,char}$ are characteristic or freestream flow properties. The laminar Reynolds number is estimated by:

$$Re = \frac{\rho_{char} V_{initial} L_{REF}}{\mu_{m,char}} , \tag{61}$$

with L_{REF} a characteristic configuration length. The magnetic Reynolds number is calculated by:

$$Re_\sigma = L_{REF} V_{initial} \mu_{M,char} \sigma_{char} . \tag{62}$$

The components of the Joule heat flux vector, which characterizes the non-ideal formulation, are determined by:

$$q_{J,x} = -R_b\left\{\frac{B_y}{\mu_M\sigma}\left[\frac{\partial}{\partial x}\left(\frac{B_y}{\mu_M}\right) - \frac{\partial}{\partial y}\left(\frac{B_x}{\mu_M}\right)\right]\right\} \text{ and } q_{J,y} = -R_b\left\{\frac{B_x}{\mu_M\sigma}\left[\frac{\partial}{\partial y}\left(\frac{B_x}{\mu_M}\right) - \frac{\partial}{\partial x}\left(\frac{B_y}{\mu_M}\right)\right]\right\} . \tag{63}$$

5. Turbulence Models
Five turbulence models were implemented according to a k-ω and $k^{1/2}$-ω formulations. Details of the five turbulence models are found in [42,43]. The interested reader is encouraged to read these references to become aware of the numerical implementation of such models.

6. Maciel Centered Scheme
Maciel centered scheme is obtained by arithmetical average between the flux at the left and right states of the interface. Considering the two-dimensional and structured case, the algorithm is divided in three parts, as recommended by [44], each one corresponding to a characteristic flux. The first part takes into account the

dynamic part, which considers the Navier-Stokes equations plus the Maxwell equations and the four equations of the turbulence model, the second one takes into account the chemical part, and the third part takes into account the vibrational part. Hence, the discrete-dynamic-convective flux, which solves the dynamic part, is given by Eq. (64).

$$
R_{i+1/2,j}^{Dyn} = \frac{1}{2}\left[\begin{pmatrix}
\rho u \\
\rho u^2 + P - R_b\,B_x^2/\mu_M \\
\rho uv - R_b\,B_x B_y/\mu_M \\
(\rho Z + P)u - R_b(\vec{V}\bullet\vec{B}/\mu_M)B_x \\
\rho ku \\
\rho\omega u \\
\rho Q_h u \\
\rho Q_s u \\
0 \\
uB_y - vB_x
\end{pmatrix}_L + \begin{pmatrix}
\rho u \\
\rho u^2 + P - R_b\,B_x^2/\mu_M \\
\rho uv - R_b\,B_x B_y/\mu_M \\
(\rho Z + P)u - R_b(\vec{V}\bullet\vec{B}/\mu_M)B_x \\
\rho ku \\
\rho\omega u \\
\rho Q_h u \\
\rho Q_s u \\
0 \\
uB_y - vB_x
\end{pmatrix}_R\right]S_x +
$$

$$
\frac{1}{2}\left[\begin{pmatrix}
\rho v \\
\rho uv - R_b B_x B_y/\mu_M \\
\rho v^2 + P - R_b\,B_y^2/\mu_M \\
(\rho Z + P)v - R_b(\vec{V}\bullet\vec{B}/\mu_M)B_y \\
\rho kv \\
\rho\omega v \\
\rho Q_h v \\
\rho Q_s v \\
vB_x - uB_y \\
0
\end{pmatrix}_L + \begin{pmatrix}
\rho v \\
\rho uv - R_b B_x B_y/\mu_M \\
\rho v^2 + P - R_b\,B_y^2/\mu_M \\
(\rho Z + P)v - R_b(\vec{V}\bullet\vec{B}/\mu_M)B_y \\
\rho kv \\
\rho\omega v \\
\rho Q_h v \\
\rho Q_s v \\
vB_x - uB_y \\
0
\end{pmatrix}_R\right]S_y ; \qquad (64)
$$

the discrete-chemical-convective flux is defined by:

$$
R_{i+1/2,j}^{Chem} = \frac{1}{2}\left[\begin{pmatrix}
\rho_1 u \\ \rho_2 u \\ \rho_4 u \\ \rho_5 u \\ \rho_6 u \\ \rho_7 u \\ \rho_8 u \\ \rho_9 u \\ \rho_{10} u \\ \rho_{11} u
\end{pmatrix}_L + \begin{pmatrix}
\rho_1 u \\ \rho_2 u \\ \rho_4 u \\ \rho_5 u \\ \rho_6 u \\ \rho_7 u \\ \rho_8 u \\ \rho_9 u \\ \rho_{10} u \\ \rho_{11} u
\end{pmatrix}_R\right]S_x + \frac{1}{2}\left[\begin{pmatrix}
\rho_1 v \\ \rho_2 v \\ \rho_4 v \\ \rho_5 v \\ \rho_6 v \\ \rho_7 v \\ \rho_8 v \\ \rho_9 v \\ \rho_{10} v \\ \rho_{11} v
\end{pmatrix}_L + \begin{pmatrix}
\rho_1 v \\ \rho_2 v \\ \rho_4 v \\ \rho_5 v \\ \rho_6 v \\ \rho_7 v \\ \rho_8 v \\ \rho_9 v \\ \rho_{10} v \\ \rho_{11} v
\end{pmatrix}_R\right]S_y ; \qquad (65)
$$

and the discrete-vibrational-convective flux is determined by:

$$
R_{i+1/2,j}^{Vib} = \frac{1}{2}\left[(\rho e_v u)_L + (\rho e_v u)_R\right]S_x + \frac{1}{2}\left[(\rho e_v v)_L + (\rho e_v v)_R\right]S_y. \qquad (66)
$$

The viscous formulation follows that of [45], which adopts the Green theorem to calculate primitive variable gradients. The viscous gradients at the interface are also obtained by arithmetical average between cell (i,j) and

its neighbors. As it was done with the convective terms, there is a need to separate the viscous flux in three parts: dynamical viscous flux, chemical viscous flux and vibrational viscous flux. The dynamical part corresponds to:

$$
R_{i+1/2,j}^{Dyn} = \frac{1}{2}\left[\begin{pmatrix} 0 \\ (t_{xx}+\tau_{xx})/Re \\ (t_{xy}+\tau_{xy})/Re \\ (f_x-\phi_x)/Re - q_{J,x}/Re_\sigma \\ \alpha_x/Re \\ \beta_x/Re \\ \gamma_x/Re \\ \delta_x/Re \\ 0 \\ \frac{1}{Re_\sigma}\frac{1}{\sigma}\left[\frac{\partial}{\partial x}\left(\frac{B_y}{\mu_M}\right)-\frac{\partial}{\partial y}\left(\frac{B_x}{\mu_M}\right)\right] \end{pmatrix}_L + \begin{pmatrix} 0 \\ (t_{xx}+\tau_{xx})/Re \\ (t_{xy}+\tau_{xy})/Re \\ (f_x-\phi_x)/Re - q_{J,x}/Re_\sigma \\ \alpha_x/Re \\ \beta_x/Re \\ \gamma_x/Re \\ \delta_x/Re \\ 0 \\ \frac{1}{Re_\sigma}\frac{1}{\sigma}\left[\frac{\partial}{\partial x}\left(\frac{B_y}{\mu_M}\right)-\frac{\partial}{\partial y}\left(\frac{B_x}{\mu_M}\right)\right] \end{pmatrix}_R\right] S_x +
$$

$$
\frac{1}{2}\left[\begin{pmatrix} 0 \\ (t_{xy}+\tau_{xy})/Re \\ (t_{yy}+\tau_{yy})/Re \\ (f_y-\phi_y)/Re - q_{J,y}/Re_\sigma \\ \alpha_y/Re \\ \beta_y/Re \\ \gamma_y/Re \\ \delta_y/Re \\ \frac{1}{Re_\sigma}\frac{1}{\sigma}\left[\frac{\partial}{\partial y}\left(\frac{B_x}{\mu_M}\right)-\frac{\partial}{\partial x}\left(\frac{B_y}{\mu_M}\right)\right] \\ 0 \end{pmatrix}_L + \begin{pmatrix} 0 \\ (t_{xy}+\tau_{xy})/Re \\ (t_{yy}+\tau_{yy})/Re \\ (f_y-\phi_y)/Re - q_{J,y}/Re_\sigma \\ \alpha_y/Re \\ \beta_y/Re \\ \gamma_y/Re \\ \delta_y/Re \\ \frac{1}{Re_\sigma}\frac{1}{\sigma}\left[\frac{\partial}{\partial y}\left(\frac{B_x}{\mu_M}\right)-\frac{\partial}{\partial x}\left(\frac{B_y}{\mu_M}\right)\right] \\ 0 \end{pmatrix}_R\right] S_y ;
\tag{67}
$$

To the chemical part one has:

$$
R_{i+1/2,j}^{Chem} = \frac{1}{2}\left[\begin{pmatrix} (-\rho_1 v_{1x}-\theta_{1x})/Re \\ (-\rho_2 v_{2x}-\theta_{2x})/Re \\ (-\rho_4 v_{4x}-\theta_{4x})/Re \\ (-\rho_5 v_{5x}-\theta_{5x})/Re \\ (-\rho_6 v_{6x}-\theta_{6x})/Re \\ (-\rho_7 v_{7x}-\theta_{7x})/Re \\ (-\rho_8 v_{8x}-\theta_{8x})/Re \\ (-\rho_9 v_{9x}-\theta_{9x})/Re \\ (-\rho_{10} v_{10x}-\theta_{10x})/Re \\ (-\rho_{11} v_{11x}-\theta_{11x})/Re \end{pmatrix}_L + \begin{pmatrix} (-\rho_1 v_{1x}-\theta_{1x})/Re \\ (-\rho_2 v_{2x}-\theta_{2x})/Re \\ (-\rho_4 v_{4x}-\theta_{4x})/Re \\ (-\rho_5 v_{5x}-\theta_{5x})/Re \\ (-\rho_6 v_{6x}-\theta_{6x})/Re \\ (-\rho_7 v_{7x}-\theta_{7x})/Re \\ (-\rho_8 v_{8x}-\theta_{8x})/Re \\ (-\rho_9 v_{9x}-\theta_{9x})/Re \\ (-\rho_{10} v_{10x}-\theta_{10x})/Re \\ (-\rho_{11} v_{11x}-\theta_{11x})/Re \end{pmatrix}_R\right] S_x +
$$

$$\frac{1}{2}\left[\begin{pmatrix} \left(-\rho_1 v_{1y} - \theta_{1y}\right)/\text{Re} \\ \left(-\rho_2 v_{2y} - \theta_{2y}\right)/\text{Re} \\ \left(-\rho_4 v_{4y} - \theta_{4y}\right)/\text{Re} \\ \left(-\rho_5 v_{5y} - \theta_{5y}\right)/\text{Re} \\ \left(-\rho_6 v_{6y} - \theta_{6y}\right)/\text{Re} \\ \left(-\rho_7 v_{7y} - \theta_{7y}\right)/\text{Re} \\ \left(-\rho_8 v_{8y} - \theta_{8y}\right)/\text{Re} \\ \left(-\rho_9 v_{9y} - \theta_{9y}\right)/\text{Re} \\ \left(-\rho_{10} v_{10y} - \theta_{10y}\right)/\text{Re} \\ \left(-\rho_{11} v_{11y} - \theta_{11y}\right)/\text{Re} \end{pmatrix}_L + \begin{pmatrix} \left(-\rho_1 v_{1y} - \theta_{1y}\right)/\text{Re} \\ \left(-\rho_2 v_{2y} - \theta_{2y}\right)/\text{Re} \\ \left(-\rho_4 v_{4y} - \theta_{4y}\right)/\text{Re} \\ \left(-\rho_5 v_{5y} - \theta_{5y}\right)/\text{Re} \\ \left(-\rho_6 v_{6y} - \theta_{6y}\right)/\text{Re} \\ \left(-\rho_7 v_{7y} - \theta_{7y}\right)/\text{Re} \\ \left(-\rho_8 v_{8y} - \theta_{8y}\right)/\text{Re} \\ \left(-\rho_9 v_{9y} - \theta_{9y}\right)/\text{Re} \\ \left(-\rho_{10} v_{10y} - \theta_{10y}\right)/\text{Re} \\ \left(-\rho_{11} v_{11y} - \theta_{11y}\right)/\text{Re} \end{pmatrix}_R \right] S_y ; \tag{68}$$

Finally, to the vibrational part:

$$R_{i+1/2,j}^{\text{Vib}} = \frac{1}{2}\left[\left(\frac{q_{v,x} - \phi_{v,x}}{\text{Re}}\right)_L + \left(\frac{q_{v,x} - \phi_{v,x}}{\text{Re}}\right)_R\right] S_x + \frac{1}{2}\left[\left(\frac{q_{v,y} - \phi_{v,y}}{\text{Re}}\right)_L + \left(\frac{q_{v,y} - \phi_{v,y}}{\text{Re}}\right)_R\right] S_y . \tag{69}$$

where $S_{i+1/2,j} = \begin{bmatrix} S_x & S_y \end{bmatrix}_{i+1/2,j}^t$ defines the normal area vector for the surface (i+½,j). The normal area components S_x and S_y to each flux interface are given in Tab. 1. Figure 1 exhibits the computational cell adopted for the simulations, as well its respective nodes and flux interfaces.

The resultant ordinary differential equation system can be written as:

$$V_{i,j}\, dQ_{i,j}/dt = -\left(R_{i,j-1/2} + R_{i+1/2,j} + R_{i,j+1/2} + R_{i-1/2,j}\right) = -C_{i,j}, \tag{70}$$

where the cell volume is given by:

$$V_{i,j} = 0.5\left|\left(x_{i,j} - x_{i+1,j}\right)y_{i+1,j+1} + \left(x_{i+1,j} - x_{i+1,j+1}\right)y_{i,j} + \left(x_{i+1,j+1} - x_{i,j}\right)y_{i+1,j}\right| +$$
$$0.5\left|\left(x_{i,j} - x_{i+1,j+1}\right)y_{i,j+1} + \left(x_{i+1,j+1} - x_{i,j+1}\right)y_{i,j} + \left(x_{i,j+1} - x_{i,j}\right)y_{i+1,j+1}\right| . \tag{71}$$

This centered scheme is second order accurate in space, according to a finite difference discretization, and needs an artificial dissipation operator, D, to guarantee stability in presence of shock waves and background instabilities. Considering this operator, Eq. (70) can be rewritten as:

$$dQ_{i,j}/dt = -\left(C_{i,j} - D_{i,j}\right)/V_{i,j} , \tag{72}$$

where D has the following structure:

$$D\left(Q_{i,j}\right) = d^{(2)}\left(Q_{i,j}\right) - d^{(4)}\left(Q_{i,j}\right), \tag{73}$$

with:

$$d^{(2)} = 0.5\varepsilon_{i,j-1/2}^{(2)}\left(A_{i,j} + A_{i,j-1}\right)\left(Q_{i,j-1} - Q_{i,j}\right) + 0.5\varepsilon_{i+1/2,j}^{(2)}\left(A_{i,j} + A_{i+1,j}\right)\left(Q_{i+1,j} - Q_{i,j}\right) +$$
$$0.5\varepsilon_{i,j+1/2}^{(2)}\left(A_{i,j} + A_{i,j+1}\right)\left(Q_{i,j+1} - Q_{i,j}\right) + 0.5\varepsilon_{i-1/2,j}^{(2)}\left(A_{i,j} + A_{i-1,j}\right)\left(Q_{i-1,j} - Q_{i,j}\right) \tag{74}$$

named the undivided Laplacian operator, responsible by the numerical stability in presence of shock waves; and

$$d^{(4)} = 0.5\varepsilon_{i,j-1/2}^{(4)}\left(A_{i,j} + A_{i,j-1}\right)\left(\nabla^2 Q_{i,j-1} - \nabla^2 Q_{i,j}\right) +$$
$$0.5\varepsilon_{i+1/2,j}^{(4)}\left(A_{i,j} + A_{i+1,j}\right)\left(\nabla^2 Q_{i+1,j} - \nabla^2 Q_{i,j}\right) +$$
$$0.5\varepsilon_{i,j+1/2}^{(4)}\left(A_{i,j} + A_{i,j+1}\right)\left(\nabla^2 Q_{i,j+1} - \nabla^2 Q_{i,j}\right) +$$
$$0.5\varepsilon_{i-1/2,j}^{(4)}\left(A_{i,j} + A_{i-1,j}\right)\left(\nabla^2 Q_{i-1,j} - \nabla^2 Q_{i,j}\right), \tag{75}$$

named the bi-harmonic operator, responsible by the background stability (odd-even instabilities, for instance). In this last term,

$$\nabla^2 Q_{i,j} = \left(Q_{i,j-1} - Q_{i,j}\right) + \left(Q_{i+1,j} - Q_{i,j}\right) + \left(Q_{i,j+1} - Q_{i,j}\right) + \left(Q_{i-1,j} - Q_{i,j}\right). \tag{76}$$

In the $d^{(4)}$ operator, $\nabla^2 Q_{i,j}$ is extrapolated from your neighbor cell every time that such one represents an especial boundary layer cell, recognized in the CFD literature as "ghost" cell. The ε terms are defined, for instance, as:

$$\varepsilon_{i,j-1/2}^{(2)} = K^{(2)} MAX\left(\nu_{i,j}, \nu_{i,j-1}\right) \text{ and } \varepsilon_{i,j-1/2}^{(4)} = MAX\left[0, \left(K^{(4)} - \varepsilon_{i,j-1/2}^{(2)}\right)\right], \tag{77}$$

in which:

$$\nu_{i,j} = \left(\left|p_{i,j-1} - p_{i,j}\right| + \left|p_{i+1,j} - p_{i,j}\right| + \left|p_{i,j+1} - p_{i,j}\right| + \left|p_{i-1,j} - p_{i,j}\right|\right) / \left(p_{i,j-1} + p_{i+1,j} + p_{i,j+1} + p_{i-1,j} + 4p_{i,j}\right). \tag{78}$$

represents a pressure sensor employed to identify regions of high gradients. Each time that a neighbor cell represents a ghost cell, it is assumed that, for instance, $\nu_{ghost} = \nu_{i,j}$. The $A_{i,j}$ terms define the particular artificial dissipation operator. Two models were studied in the current work:

(a)   Artificial dissipation operator of Mavriplis / Scalar, non-linear, and isotropic model:

In this case, the $A_{i,j}$ terms represent the sum of the contributions of the maximum normal eigenvalue associated to the flux interface of the Euler equations, integrated along each cell face. Based on [46] work, these terms are defined as:

$$A_{i,j} = \left|u_{int}S_x + v_{int}S_y\right|_{i,j-1/2} + a_{int}\left(S_x^2 + S_y^2\right)_{i,j-1/2}^{0.5} + \left|u_{int}S_x + v_{int}S_y\right|_{i+1/2,j} + a_{int}\left(S_x^2 + S_y^2\right)_{i+1/2,j}^{0.5} +$$

$$\left|u_{int}S_x + v_{int}S_y\right|_{i,j+1/2} + a_{int}\left(S_x^2 + S_y^2\right)_{i,j+1/2}^{0.5} + \left|u_{int}S_x + v_{int}S_y\right|_{i-1/2,j} + a_{int}\left(S_x^2 + S_y^2\right)_{i-1/2,j}^{0.5}, \tag{79}$$

where "a" represents the sound speed and the interface properties are evaluated by arithmetical average. The $K^{(2)}$ and $K^{(4)}$ constants have typical values of 1/4 and 3/256, respectively.

(b)   Artificial dissipation model of Turkel and Vatsa / Scalar, non-linear, and anisotropic model:

The aforementioned artificial dissipation model presents the characteristic of being isotropic. In words, the dissipation introduced artificially in a given coordinate direction to stabilize the scheme weights equally the phenomena originated from all directions, having not a more significant weighting from the particular direction under study. The dissipation is clearly isotropic. The scalar, non-linear and anisotropic artificial dissipation model of [47] aims to provide a numerical attenuation that considers with bigger weight the propagation information effects associated to the characteristic maximum eigenvalue from the coordinate direction under study. Basically, such artificial dissipation model differs from the non-linear, isotropic model of [46] only in the determination of the weighting term of the dissipation operator.

$$A_\xi = \overline{\lambda}_{\xi_{i+1/2,j}}\left[1 + \left(\overline{\lambda}_\eta \middle/ \overline{\lambda}_\xi\right)_{i+1/2,j}^{0.5}\right], \overline{\lambda}_{\xi_{i+1/2,j}} = \left(\left|un_x + vn_y\right| + a\right)_{i+1/2,j} S_{i+1/2,j} \text{ and }$$

$$\overline{\lambda}_{\eta_{i+1/2,j}} = \left(\left|un_x + vn_y\right| + a\right)_{i+1/2,j} S_{i+1/2,j}; \tag{80}$$

$$A_\eta = \overline{\lambda}_{\eta_{i,j+1/2}}\left[1 + \left(\overline{\lambda}_\xi \middle/ \overline{\lambda}_\eta\right)_{i,j+1/2}^{0.5}\right], \overline{\lambda}_{\xi_{i,j+1/2}} = \left(\left|un_x + vn_y\right| + a\right)_{i,j+1/2} S_{i,j+1/2} \text{ and }$$

$$\overline{\lambda}_{\eta_{i,j+1/2}} = \left(\left|un_x + vn_y\right| + a\right)_{i,j+1/2} S_{i,j+1/2}. \tag{81}$$

To this artificial dissipation model, the recommended values of $K^{(2)}$ and $K^{(4)}$ by [47] are 1/2 and 1/64, respectively.

7.   Time Integration

Three methods of time integration were studied herein, namely: Euler Backward, Middle Point, and Runge-Kutta 4th Order. For details of such implementation, the reader is encouraged to read [43].

8. Spatially Variable Time Step

The spatially variable time step has proved efficient gains in terms of convergence acceleration, as proved by [27-28]. Initially, the parameter σ is determined, where:

$$\sigma_s = \frac{c_s}{M_s} \text{ and } \sigma = \sum_{s=1}^{N} \sigma_s ,$$

(82)

with c_s being the mass fraction and M_s the molecular weight. The total specific heat at constant volume due to translation is defined as:

$$c_{V,T} = \sum_{s=1}^{N} \sigma_s c_{V,T,s} ,$$

(83)

where, for each gas constituent of the eleven (11) species chemical model, the specific heat at constant volume, based on the kinetic theory of gases [48], is defined by

$$c_{V,T,N} = \frac{3}{2}R_N , \; c_{V,T,O} = \frac{3}{2}R_O , \; c_{V,T,N_2} = \frac{5}{2}R_{N_2} , \; c_{V,T,O_2} = \frac{5}{2}R_{O_2} , \; c_{V,T,NO} = \frac{5}{2}R_{NO} ;$$

$$c_{V,T,N^+} = \frac{3}{2}R_{N^+} , \; c_{V,T,O^+} = \frac{3}{2}R_{O^+} , \; c_{V,T,N_2^+} = \frac{5}{2}R_{N_2^+} , \; c_{V,T,O_2^+} = \frac{5}{2}R_{O_2^+} , \; c_{V,T,NO^+} = \frac{5}{2}R_{NO^+} ;$$

$$c_{V,T,e^-} = \frac{3}{2}R_{e^-} .$$

(84)

Being R_s the specific gas constant. The total pressure of the gaseous mixture is determined by Dalton law, which indicates that the total pressure of the gas is the sum of the partial pressure of each constituent gas, resulting in:

$$p_s = c_s \rho R_s T \text{ and } p = \sum_{s=1}^{N} p_s .$$

(85)

The speed of sound to a reactive mixture considering the two-equation turbulence models can be determined by:

$$a = \sqrt{\frac{(1+\beta)p}{\rho} - k} ,$$

(86)

where $\beta = \dfrac{R_{univ}\sigma}{c_{V,T}}$, with R_{univ} = 1.987 cal/(g-mol.K). Finally, the spatially variable time step is defined from the CFL (Courant-Friedrichs-Lewis) definition:

$$\Delta t_{i,j} = \frac{CFL \Delta s_{i,j}}{\sqrt{u_{i,j}^2 + v_{i,j}^2 + a_{i,j}}} ,$$

(87)

where $\Delta s_{i,j}$ is the characteristic length of each cell (defined between the minimum cell side length and the minimum centroid distance between each cell and its neighbors).

9. Dimensionless Scales, Initial and Boundary Conditions
9.1. Dimensionless Scales

The dimensionless scales employed to the reactive equations consisted in: R_s is dimensionless by a_{char}, where $a_{char} = \sqrt{\gamma p_{char}/\rho_{char}}$; c_v is dimensionless by a_{char}; h_s and Δh_s^0 are dimensionless by a_{char}^2; T and T_v, translational/rotational temperature and vibrational temperature, respectively, are dimensionless by a_{char}; ρ_s and ρ are dimensionless by ρ_{char}; u and v are dimensionless by a_{char}; μ_m is dimensionless by $\mu_{m,char}$; D, diffusion

coefficient, dimensionless by $a_{char}^2 dt_{char}$, where dt_{char} is the minimum time step calculated in the computational domain at the first iteration; $\dot{\omega}$ is dimensionless by $(\rho_{char}/dt_{char})x10^{-3}$; e_v is dimensionless by a_{char}^2; e and p are dimensionless by $\rho_{char}a_{char}^2$; τ_s, relaxation time, is dimensionless by dt_{char}. To the Maxwell equations: the B_x and B_y Cartesian components of the magnetic field dimensionless by $B_{initial}$; the magnetic permeability of the mean is dimensionless by $\mu_{M,char}$; and the electric conductivity is dimensionless by σ_{char}. The characteristic parameters are defined in [49].

9.2. Initial Condition
The initial conditions to this problem, for an eleven species chemical model, coupled with a turbulence model and suffering the actuation of a magnetic field, are presented in Tab. 2. The Reynolds number is obtained from data of [49].

9.3. Boundary Conditions
The boundary conditions are basically of three types: solid wall, entrance, and exit. These conditions are implemented with the help of ghost cells.

Wall condition. In the viscous case, the non-slip condition is enforced. Therefore, the tangent velocity component of the ghost volume at wall has the same magnitude as the respective velocity component of its real neighbor cell, but opposite signal. In the same way, the normal velocity component of the ghost volume at wall is equal in value, but opposite in signal, to the respective velocity component of its real neighbor cell. It results in:

$$u_g = -u_r \text{ and } v_g = -v_r. \tag{88}$$

where "g" indicates ghost cell properties and "r" indicates real cell properties.

The normal pressure gradient of the fluid at the wall is assumed to be equal to zero according to a boundary-layer like condition. The same hypothesis is applied for the normal temperature gradient at the wall, assuming an adiabatic wall. From these considerations, density and translational/rotational temperature are extrapolated from the respective values of its real neighbor volume (zero order extrapolation). The total vibrational internal energy is also extrapolated. The turbulent kinetic energy and the turbulent vorticity at the ghost volumes are determined by the following expressions:

$$k_{ghost} = 0.0 \text{ and } \omega_{ghost}^2 = \left[(38/3\nu_M)/(\beta d_n^2)\right]^2, \tag{89}$$

where β assumes the value 3/40 and d_n is the distance of the first cell to the wall. The Q_h and Q_s variables are fixed by their initial values.

With the mixture species mass fractions and with the values of the respective specific heats at constant volume, it is possible to obtain the mixture specific heat at constant volume. The mixture formation enthalpy is extrapolated from the real cell. The Cartesian components of the induced magnetic field at the wall to the ghost cells are fixed with their initial values. The magnetic permeability is considered constant with its initial value. The mixture total energy to the ghost cell is calculated by:

$$Z_g = c_{v,mixt,g}\left(T_{tr,g} - T_{REF}\right) + \Delta h_{mixt,g}^0 + e_{v,nond,g} + 0.5\left(u_g^2 + v_g^2\right) + R_b\left(B_{x,g}^2 + B_{y,g}^2\right)/\left(2\mu_{M,g}\rho_g\right). \tag{90}$$

To the species density, the non-catalytic condition is imposed, what corresponds to zero order extrapolation from the real cell.

Entrance condition. It is divided in two flow regimes:

(a) Subsonic flow: Seven properties are specified and three extrapolated in the boundary conditions of the dynamic part of the algorithm. This approach is based on information propagation analysis along characteristic directions in the calculation domain ([50]). In other words, for subsonic flow, seven characteristics propagate information pointing into the computational domain. Thus seven flow properties must be fixed at the inlet plane. Just three characteristic lines allow information to travel upstream. So, three flow variables must be extrapolated

from the interior grid to the inlet boundary. The total energy and the components of the magnetic field were the extrapolated variables from the real neighbor volumes, for the studied problem. Density and velocity components adopted values of the initial flow. The turbulence kinetic energy and the vorticity were fixed with the values of the initial condition. Q_h and Q_s variables are also fixed with the values $10^{-6} h_{initial}^2$ and 10^{-3}

$\sum_{i=s}^{N} c_{i,initial}^2$, respectively. To the chemical part, ten information propagate upstream because it is assumed that

all ten equations are conducted by the eigenvalue "$(q_n$-a)". In the subsonic flow, all eigenvalues are negative and the information should be extrapolated. In the same reasoning to the chemical boundary conditions, the vibrational-internal-energy equation is dictated by the "$(q_n$-a)" eigenvalue and, in the subsonic region, its value is negative. Hence, the vibrational internal energy should be extrapolated.
(b) Supersonic flow: In this case no information travels upstream; therefore all variables are fixed with their initial values.

Exit condition. It is also divided in two flow regimes:
(a) Subsonic flow: Three characteristics propagate information outward the computational domain. Hence, the associated variables should be extrapolated from interior information. The characteristic direction associated to the "$(q_{normal}$-a)" velocity should be specified because it points inward to the computational domain ([50]). In this case, the ghost volume total energy and the induced magnetic components are specified from their initial values. Density and velocity components are extrapolated. The turbulence kinetic energy and the vorticity are prescribed and receive the following values: $0.01k_{ff}$ and $10u/L_{REF}$, respectively, where k_{ff} = $0.5u^2$. Q_h and Q_s variables are also fixed with the values $10^{-6} h_{initial}^2$ and $10^{-3} \sum_{i=s}^{N} c_{i,initial}^2$, respectively. For the [13] turbulence

model, the turbulence kinetic energy is $\sqrt{0.01k_{ff}}$. To the chemical part, the eigenvalue "$(q_n$-a)" is again negative and the characteristics are always flowing into the computational domain. Hence, the ten chemical species under study should have their densities fixed by their initial values. In the same reasoning, the internal vibrational energy should have its value prescribed by its initial value due to the eigenvalue "$(q_n$-a)" be negative.
(b) Supersonic flow: All variables are extrapolated from interior grid cells, as no flow information can make its way upstream. In other words, nothing can be fixed.

10. Physical Problem and Mesh
Firstly the blunt body problem is studied. The geometry under study is a blunt body with 1.0 m of nose ratio and parallel rectilinear walls. The far field is located at 20.0 times the nose ratio in relation to the configuration nose. Figure 2 shows the viscous mesh used to the blunt body physical problem. This mesh is composed of 2,548 rectangular cells and 2,650 nodes. This mesh is equivalent in finite differences to a one of 53x50 points. An exponential stretching of 5.0% in the η direction was used to the viscous simulations. A "O" mesh is taken as the base to construct such mesh. No smoothing is used in this mesh generation process, being this one constructed in Cartesian coordinates.

11. Results
Tests were performed in a Core i7 processor of 2.1GHz and 8.0Gbytes of RAM microcomputer, in a Windows 8.0 environment. Three (3) orders of reduction of the maximum residual in the field were considered to obtain a converged solution. The residual was defined as the value of the discretized conservation equation. In the dynamic part, such definition results in:

$$\text{Residual} \quad = \quad -\Delta t_{i,j} / V_{i,j} \times \left(C_{i,j} - D_{i,j} \right). \tag{91}$$

The attack angle was adopted equal to zero. Only the [46] artificial dissipation model yielded converged solutions.

11.1. Euler Backward

Coakley (1983) results. Figures 3 to 6 exhibit the pressure and N_2 mass fraction contours obtained by the Maciel scheme as using the [29] and [30] chemical models coupled with the [13] turbulence model. The Maciel scheme captures the normal shock wave with good resolution. The shock wave captured by the Maciel scheme using the [29] chemical model is more severe than that obtained with the [30] chemical model. Good symmetry and homogeneous properties are observed. Good dissociation of N_2 is perceptible for both chemical models. Some oscillations are noted in the mass fraction contours. The dissociation of N_2 with the [29] chemical model is bigger than the respective dissociation with the [30] chemical model.

Wilcox (1988) results. Figures 7 to 10 show the pressure and N_2 mass fraction contours obtained by the Maciel scheme as using the [29] and [30] chemical models coupled with the [14] turbulence model. The Maciel scheme captures accurately the normal shock wave. The shock wave captured by the Maciel scheme using the [29] chemical model is again more severe than that obtained with the [30] chemical model. Good symmetry and homogeneous properties are observed. Good dissociation of N_2 is perceptible for both chemical models. Some oscillations are perceptible in the mass fraction contours.

Yoder, Georgiadids and Orkwis (1996). Figures 11 to 14 show the pressure and N_2 mass fraction contours obtained by the Maciel scheme as using the [29] and [30] chemical models coupled with the [15] turbulence model. The Maciel scheme captures again the normal shock wave with precision. The shock wave captured by the Maciel scheme using the [29] chemical model is again more severe than that obtained with the [30] chemical model. Good symmetry properties are observed. Good dissociation of N_2 is perceptible for both chemical models. Some oscillations are observed in the mass fraction contours. The dissociation of N_2 with the [29] chemical model is bigger than the respective dissociation with the [30] chemical model.

Coakley (1997). Figures 15 to 18 show the pressure and N_2 mass fraction contours obtained by the Maciel scheme as using the [29] and [30] chemical models coupled with the [16] turbulence model. The Maciel scheme captures accurately the normal shock wave. The shock wave captured by the Maciel scheme using the [29] chemical model is again more strength. Good symmetry and homogeneous properties are observed. Good dissociation of N_2 is perceptible for both chemical models. Some oscillations are noted in the mass fraction contours.

Rumsey, Gatski, Ying and Bertelrud (1998). Figures 19 to 22 show the pressure and N_2 mass fraction contours obtained by the Maciel scheme as using the [29] and [30] chemical models coupled with the [17] turbulence model. The Maciel scheme captures the normal shock wave with good precision. The shock wave captured by the Maciel scheme using the [29] chemical model is again more strength. Good symmetry properties are observed. Good dissociation of N_2 is perceptible. Some oscillations are verified in the mass fraction contours. The dissociation of N_2 with the [29] chemical model is bigger than the respective dissociation with the [30] chemical model.

11.2. Middle Point

Coakley (1983) results. Figures 23 to 26 exhibit the pressure and N_2 mass fraction contours obtained by the Maciel scheme as using the [29] and [30] chemical models coupled with the [13] turbulence model. The Maciel scheme captures the normal shock wave with good precision. The shock wave captured by the Maciel scheme using the [29] chemical model is more severe. Good symmetry properties are observed. Good dissociation of N_2 is perceptible. Some oscillations are verified in the mass fraction contours.

Wilcox (1988) results. Figures 27 to 30 show the pressure and N_2 mass fraction contours obtained by the Maciel scheme as using the [29] and [30] chemical models coupled with the [14] turbulence model. The Maciel scheme captures accurately the normal shock wave. The shock wave captured by the Maciel scheme using the [29] chemical model is again more strength than that obtained with the [30] chemical model. Good symmetry and homogeneous properties are observed. Good dissociation of N_2 is perceptible. Some oscillations are verified in the mass fraction contours. The dissociation of N_2 with the [29] chemical model is bigger than the respective dissociation with the [30] chemical model.

Yoder, Georgiadids and Orkwis (1996). Figures 31 to 34 show the pressure and N_2 mass fraction contours obtained by the Maciel scheme as using the [29] and [30] chemical models coupled with the [15] turbulence

model. The Maciel scheme captures again the normal shock wave with precision. The shock wave captured by the Maciel scheme using the [29] chemical model is again more strength. Good symmetry properties are observed. Good dissociation of N_2 is perceptible. Some oscillations are noted in the mass fraction contours.

Coakley (1997). Figures 35 to 38 show the pressure and N_2 mass fraction contours obtained by the Maciel scheme as using the [29] and [30] chemical models coupled with the [16] turbulence model. The Maciel scheme captures the normal shock wave with good resolution. The shock wave captured by the Maciel scheme using the [29] chemical model is again more severe. Good symmetry and homogeneous properties are observed. Good dissociation of N_2 is perceptible. Some oscillations are observed in the mass fraction contours. The dissociation of N_2 with the [29] chemical model is bigger than the respective dissociation with the [30] chemical model.

Rumsey, Gatski, Ying and Bertelrud (1998). Figures 39 to 42 show the pressure and N_2 mass fraction contours obtained by the Maciel scheme as using the [29] and [30] chemical models coupled with the [17] turbulence model. The Maciel scheme captures the normal shock wave with accuracy. The shock wave captured by the Maciel scheme using the [29] chemical model is more strength. Good symmetry properties are observed. Good dissociation of N_2 is observed. Some oscillations are perceptible in the mass fraction contours.

11.3. Runge-Kutta 4th

Coakley (1983) results. Figures 43 to 46 exhibit the pressure and N_2 mass fraction contours obtained by the Maciel scheme as using the [29] and [30] chemical models coupled with the [13] turbulence model. The Maciel scheme captures the normal shock wave with accuracy. The shock wave captured by the Maciel scheme using the [29] chemical model is more strength than that obtained with the [30] chemical model. Good symmetry properties are observed. Good dissociation of N_2 is perceptible. Some oscillations are noted in the mass fraction contours. The dissociation of N_2 with the [29] chemical model is bigger than the respective dissociation with the [30] chemical model.

Wilcox (1988) results. Figures 47 to 50 show the pressure and N_2 mass fraction contours obtained by the Maciel scheme as using the [29] and [30] chemical models coupled with the [14] turbulence model. The Maciel scheme captures accurately the normal shock wave. The shock wave captured by the Maciel scheme using the [29] chemical model is again more severe. Good symmetry properties are observed. Good dissociation of N_2 is perceptible. Some oscillations are verified in the mass fraction contours.

Yoder, Georgiadids and Orkwis (1996). Figures 51 to 54 show the pressure and N_2 mass fraction contours obtained by the Maciel scheme as using the [29] and [30] chemical models coupled with the [15] turbulence model. The Maciel scheme captures again accurately the normal shock wave. The shock wave captured by the Maciel scheme using the [29] chemical model is more intense. Good symmetry and homogeneous properties are observed. Good dissociation of N_2 is perceptible. Some oscillations are noted in the mass fraction contours. The dissociation of N_2 with the [29] chemical model is bigger than the respective dissociation with the [30] chemical model.

Coakley (1997). Figures 55 to 58 show the pressure and N_2 mass fraction contours obtained by the Maciel scheme as using the [29] and [30] chemical models coupled with the [16] turbulence model. The Maciel scheme captures the normal shock wave with good precision. The shock wave captured by the Maciel scheme using the [29] chemical model is again more severe. Good symmetry properties are observed. Good dissociation of N_2 is verified. Some oscillations are observed in the mass fraction contours.

Rumsey, Gatski, Ying and Bertelrud (1998). Figures 59 to 62 show the pressure and N_2 mass fraction contours obtained by the Maciel scheme as using the [29] and [30] chemical models coupled with the [17] turbulence model. The Maciel scheme captures the normal shock wave with accuracy. The shock wave captured by the Maciel scheme using the [29] chemical model is more intense. Good symmetry and homogeneous properties are noted. Good dissociation of N_2 is observed. Some oscillations are perceptible in the mass fraction contours. The dissociation of N_2 with the [29] chemical model is bigger than the respective dissociation with the [30] chemical model.

11.4. Quantitative Analysis

In order to perform a quantitative analysis, the present reactive results are compared to the perfect gas solutions. The stagnation pressure at the blunt body nose was evaluated assuming the perfect gas formulation. Such

parameter calculated at this way is not the best comparison, but in the absence of practical reactive results, this constitutes the best available solution.

To calculate the stagnation pressure ahead of the blunt body, [51] presents in its B Appendix values of the normal shock wave properties ahead of the configuration. The ratio pr_0/pr_∞ is estimated as function of the normal Mach number and the stagnation pressure pr_0 can be determined from this parameter. Hence, to a freestream Mach number of 8.78, the ratio pr_0/pr_∞ assumes the value 99.98. The value of pr_∞ is determined by the following expression:

$$pr_\infty = \frac{pr_{initial}}{\rho_{char} \times a_{char}^2} . \tag{92}$$

In the present study, $pr_{initial} = 687N/m^2$, $\rho_{char} = 0.004kg/m^3$ and $a_{char} = 317.024m/s$. Considering these values, one concludes that $pr_\infty = 1.709$ (non-dimensional). Using the ratio obtained from [51], the stagnation pressure ahead of the configuration nose is estimated as 170.87 unities. Tables 3 and 4 compare the values of the stagnation pressure obtained from the simulations with this theoretical value and show the percentage errors. Table 3 exhibits the results for the [29] chemical model and Tab. 4 the results for the [30] chemical model. As can be seen, the best result is provided by the [29] chemical model coupled with the [13] turbulence model, in all three time marching methods, with an error of 3.56%, inferior to 5.00%.

As the hypersonic flow along the blunt body was simulated with a zero value to the attack angle, a zero lift coefficient is the expected value for this aerodynamic coefficient. Tables 5 and 6, for the [29] chemical model and for the [30] chemical model, respectively, exhibits an analysis of the lift aerodynamic coefficient, based only on pressure contribution, in this study. As can be observed, the best value to the lift coefficient is obtained by the Maciel scheme when using the [29] chemical model, coupled with the [13] turbulence model, employing the Middle Point time marching method.

11.5. Computational Performance

Tables 7 and 8, for the [29] chemical model and for the [30] chemical model, respectively, presents the computational data of the Maciel scheme for the blunt body problem. It shows the CFL number and the number of iterations to convergence for all studied cases in the current work. It can be verified that the best performance of the Maciel scheme occurred when using the [30] chemical model coupled with the [16] turbulence model and employing the Middle Point time marching method. It converged in 5,355 iterations, using a CFL of 0.05.

As final conclusion, it is possible to highlight the Maciel scheme employing the [29] chemical model coupled with the [13] turbulence model as the best performance in estimating the stagnation pressure ahead of the blunt body for all time marching methods. The best value to the lift coefficient was again obtained by the [29] chemical model coupled with the [13] turbulence model, employing the Middle Point method to march in time. Moreover, the Maciel scheme employing the [30] chemical model coupled with the [16] turbulence model, using the Middle Point method to march in time, was the most efficient in terms of computational effort. It is also important to note that both chemical models coupled with all turbulence models predicted the stagnation pressure value with errors inferior to 5.00%.

It is important to emphasize the result above where errors inferior to 5.00% were obtained for the estimation of the stagnation pressure. In the [43] work, similar studies were performed for a seven species chemical model, considering the five turbulence models studied herein and the same magnetic formulation. Errors close to 10.00% were found. Comparing these studies, it is evident that an eleven species chemical model was more realistic and represents better the flow field. With errors inferior to 5.00%, the present formulation is better than the seven species chemical model studied in [43] and is recommended as providing better treatment of the hypersonic flow under study.

Table 1: Values of S_x and S_y

Surface	S_x	S_y
i,j-1/2	$\left(y_{i+1,j} - y_{i,j} \right)$	$\left(x_{i,j} - x_{i+1,j} \right)$
i+1/2,j	$\left(y_{i+1,j+1} - y_{i+1,j} \right)$	$\left(x_{i+1,j} - x_{i+1,j+1} \right)$

| i,j+1/2 | $(y_{i,j+1} - y_{i+1,j+1})$ | $(x_{i+1,j+1} - x_{i,j+1})$ |
| i-1/2,j | $(y_{i,j} - y_{i,j+1})$ | $(x_{i,j+1} - x_{i,j})$ |

Table 2: Initial conditions to the problem of the blunt body

Property	Value
$M_{initial}$	8.78
$\rho_{initial}$	0.00326 kg/m^3
$pr_{initial}$	687 Pa
$U_{initial}$	4,776 m/s
$T_{initial}$	694 K
$T_{v,initial}$	694 K
T_{REF}	0.0 K
Altitude	40,000 m
c_N	10^{-9}
c_O	0.07955
c_{O2}	0.13400
c_{NO}	0.05090
c_{N+}	0.0
c_{O+}	0.0
c_{N2+}	0.0
c_{O2+}	0.0
c_{NO+}	0.0
c_{e-}	0.0
L_{REF}	2.0 m
Re_{char}	2.386×10^6
$k_{initial}$	10^{-6}
$\omega_{initial}$	$10 U_{initial}/L_{REF}$
$Q_{h,initial}$	$10^{-4} h_{initial}^2$
$Q_{s,initial}$	$10^{-2} \sum_{i=s}^{N} c_{i,initial}^2$
$B_{y,initial}$	0.15 T
$\mu_{M,char}$	1.2566×10^{-6}T.m/A
σ_{char}	1,000 ohm/m

Table 3: Values of stagnation pressure and respective errors (Dunn and Kang)

March Method:	Turbulence Model:	Pr$_0$:	Error:
	Coakley (1983)	164.79	3.56
	Wilcox (1988)	164.13	3.94
Euler Backward	Yoder, Georgiadids and Orkwis (1996)	163.97	4.04
	Coakley (1997)	164.14	3.94
	Rumsey, Gatski, Ying and Bertelrud (1998)	164.14	3.94
	Coakley (1983)	164.79	3.56
	Wilcox (1988)	164.13	3.94
Middle Point	Yoder, Georgiadids and Orkwis (1996)	163.97	4.04
	Coakley (1997)	164.14	3.94
	Rumsey, Gatski, Ying and Bertelrud (1998)	164.14	3.94
	Coakley (1983)	164.79	3.56
	Wilcox (1988)	164.13	3.94

Runge-Kutta 4th	Yoder, Georgiadids and Orkwis (1996)	163.97	4.04
	Coakley (1997)	164.14	3.94
	Rumsey, Gatski, Ying and Bertelrud (1998)	164.14	3.94

Table 4: Values of stagnation pressure and respective errors (Park)

March Method:	Turbulence Model:	Pr$_0$:	Error:
Euler Backward	Coakley (1983)	164.69	3.62
	Wilcox (1988)	163.98	4.03
	Yoder, Georgiadids and Orkwis (1996)	163.82	4.13
	Coakley (1997)	164.01	4.01
	Rumsey, Gatski, Ying and Bertelrud (1998)	164.01	4.01
Middle Point	Coakley (1983)	164.69	3.62
	Wilcox (1988)	163.98	4.03
	Yoder, Georgiadids and Orkwis (1996)	163.82	4.13
	Coakley (1997)	164.01	4.01
	Rumsey, Gatski, Ying and Bertelrud (1998)	164.00	4.02
Runge-Kutta 4th	Coakley (1983)	164.69	3.62
	Wilcox (1988)	163.98	4.03
	Yoder, Georgiadids and Orkwis (1996)	163.82	4.13
	Coakley (1997)	164.01	4.01
	Rumsey, Gatski, Ying and Bertelrud (1998)	164.01	4.01

Table 5: Lift aerodynamic coefficient (Dunn and Kang)

March Method:	Turbulence Model:	c$_L$:
Euler Backward	Coakley (1983)	1.6292×10^{-14}
	Wilcox (1988)	9.8966×10^{-10}
	Yoder, Georgiadids and Orkwis (1996)	3.4588×10^{-10}
	Coakley (1997)	3.4669×10^{-11}
	Rumsey, Gatski, Ying and Bertelrud (1998)	3.6340×10^{-4}
Middle Point	Coakley (1983)	7.9895×10^{-15}
	Wilcox (1988)	6.1186×10^{-10}
	Yoder, Georgiadids and Orkwis (1996)	6.8863×10^{-10}
	Coakley (1997)	-2.8299×10^{-11}
	Rumsey, Gatski, Ying and Bertelrud (1998)	3.6342×10^{-4}
Runge-Kutta 4th	Coakley (1983)	2.0727×10^{-13}
	Wilcox (1988)	-1.9664×10^{-10}
	Yoder, Georgiadids and Orkwis (1996)	-8.7393×10^{-10}
	Coakley (1997)	-4.0103×10^{-11}
	Rumsey, Gatski, Ying and Bertelrud (1998)	3.6339×10^{-4}

Table 6: Lift aerodynamic coefficient (Park)

March Method:	Turbulence Model:	c$_L$:
Euler Backward	Coakley (1983)	3.2802×10^{-13}
	Wilcox (1988)	6.6932×10^{-10}
	Yoder, Georgiadids and Orkwis (1996)	1.7756×10^{-10}
	Coakley (1997)	3.8380×10^{-11}
	Rumsey, Gatski, Ying and Bertelrud (1998)	3.6382×10^{-4}
Middle Point	Coakley (1983)	7.3049×10^{-14}
	Wilcox (1988)	3.3829×10^{-10}
	Yoder, Georgiadids and Orkwis (1996)	7.1913×10^{-10}

	Coakley (1997)		6.6547×10^{-12}
	Rumsey, Gatski, Ying and Bertelrud (1998)		3.6384×10^{-4}
	Coakley (1983)		1.5385×10^{-13}
	Wilcox (1988)		-1.8369×10^{-10}
Runge-Kutta 4th	Yoder, Georgiadids and Orkwis (1996)		3.7825×10^{-9}
	Coakley (1997)		4.6503×10^{-11}
	Rumsey, Gatski, Ying and Bertelrud (1998)		3.6382×10^{-4}

Table 7: Computational data (Dunn and Kang)

March Method:	Turbulence Model:	CFL:	Iterations:
	Coakley (1983)	0.05	5,361
	Wilcox (1988)	0.05	5,453
Euler Backward	Yoder, Georgiadids and Orkwis (1996)	0.05	5,429
	Coakley (1997)	0.05	5,362
	Rumsey, Gatski, Ying and Bertelrud (1998)	0.05	5,366
	Coakley (1983)	0.05	5,359
	Wilcox (1988)	0.05	5,451
Middle Point	Yoder, Georgiadids and Orkwis (1996)	0.05	5,427
	Coakley (1997)	0.05	5,360
	Rumsey, Gatski, Ying and Bertelrud (1998)	0.05	5,364
	Coakley (1983)	0.05	5,359
	Wilcox (1988)	0.05	5,451
Runge-Kutta 4th	Yoder, Georgiadids and Orkwis (1996)	0.05	5,427
	Coakley (1997)	0.05	5,363
	Rumsey, Gatski, Ying and Bertelrud (1998)	0.05	5,367

Table 8: Computational data (Park)

March Method:	Turbulence Model:	CFL:	Iterations:
	Coakley (1983)	0.05	5,368
	Wilcox (1988)	0.05	5,457
Euler Backward	Yoder, Georgiadids and Orkwis (1996)	0.05	5,428
	Coakley (1997)	0.05	5,356
	Rumsey, Gatski, Ying and Bertelrud (1998)	0.05	5,361
	Coakley (1983)	0.05	5,366
	Wilcox (1988)	0.05	5,455
Middle Point	Yoder, Georgiadids and Orkwis (1996)	0.05	5,426
	Coakley (1997)	0.05	5,355
	Rumsey, Gatski, Ying and Bertelrud (1998)	0.05	5,359
	Coakley (1983)	0.05	5,368
	Wilcox (1988)	0.05	5,455
Runge-Kutta 4th	Yoder, Georgiadids and Orkwis (1996)	0.05	5,427
	Coakley (1997)	0.05	5,357
	Rumsey, Gatski, Ying and Bertelrud (1998)	0.05	5,362
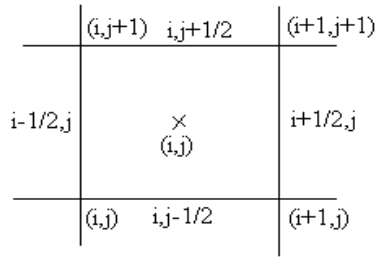
Figure 1: Computational Cell
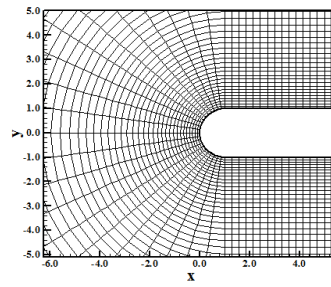
Figure 2: Blunt body viscous mesh

Euler Backward Solutions
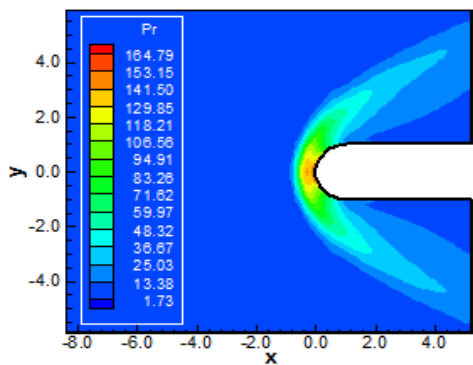
Figure 3: Pressure contours (DK-C83)
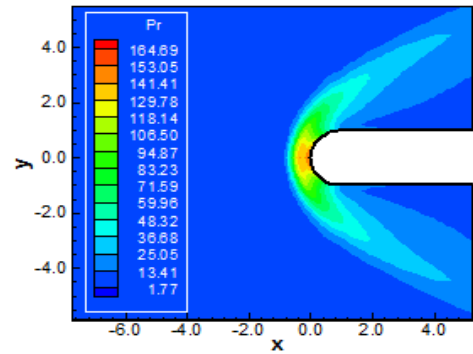
Figure 4: Pressure contours (P-C83)
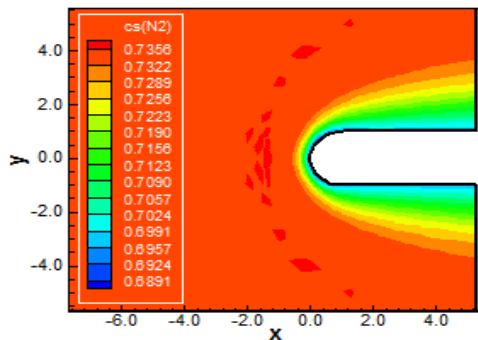
Figure 5: N_2 mass fraction contours (DK-C83)
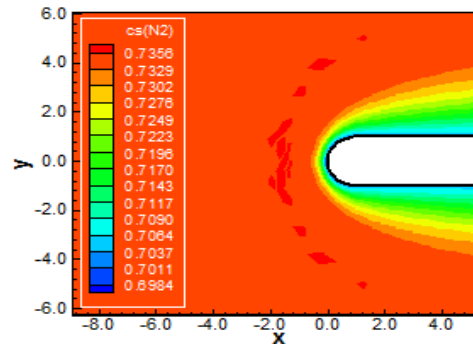
Figure 6: N_2 mass fraction contours (P-C83)
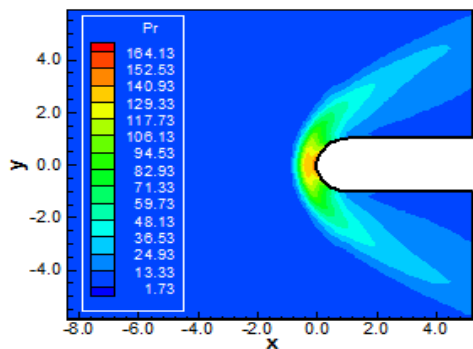
Figure 7: Pressure contours (DK-W88)
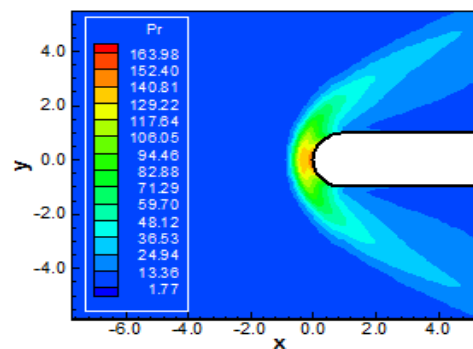
Figure 8: Pressure contours (P-C83)
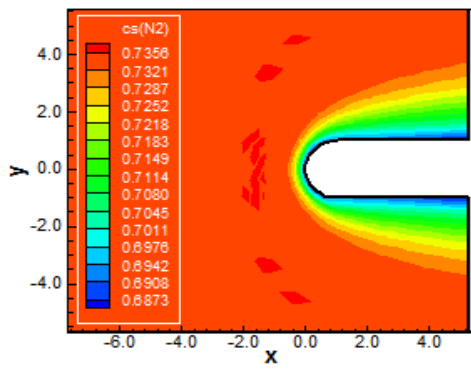
Figure 9: N₂ mass fraction contours (DK-W88)
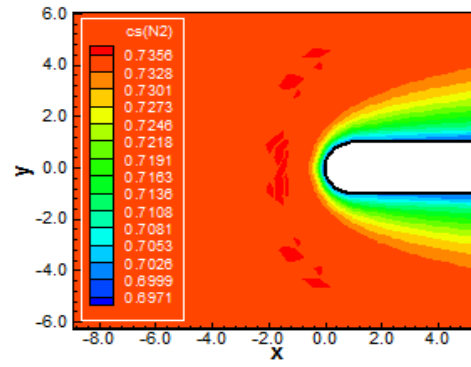
Figure 10: N₂ mass fraction contours (P-W88)
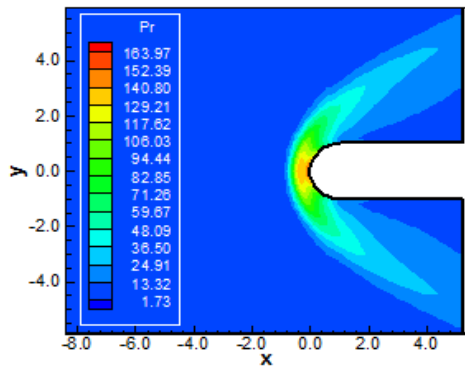
Figure 11: Pressure contours (DK-YGO96)
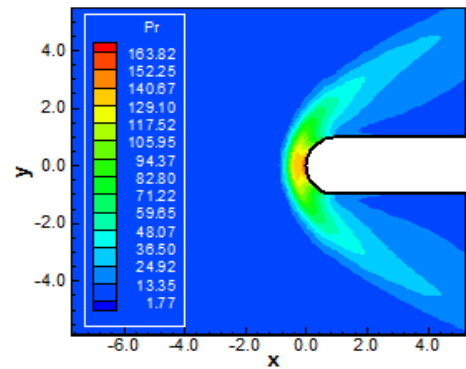
Figure 12: Pressure contours (P-YGO96)
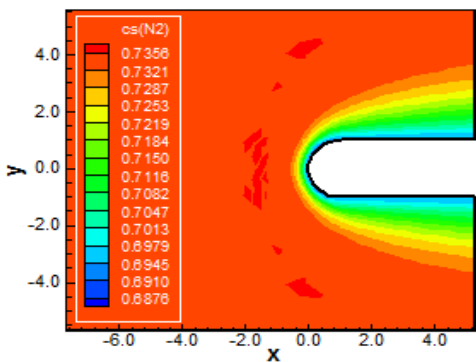
Figure 13: N₂ mass fraction contours (DK-YGO96)
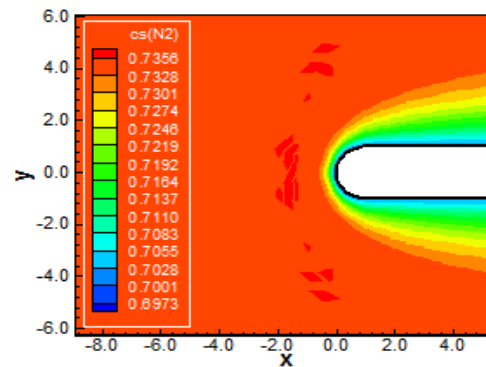
Figure 14: N₂ mass fraction contours (P-YGO96)
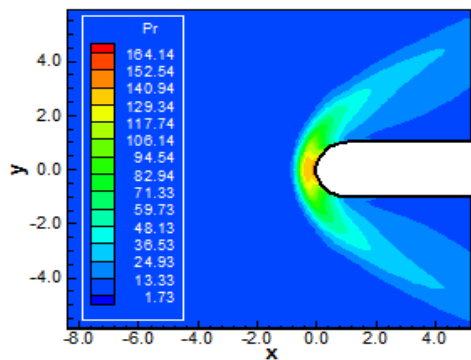
Figure 15: Pressure contours (DK-C97)
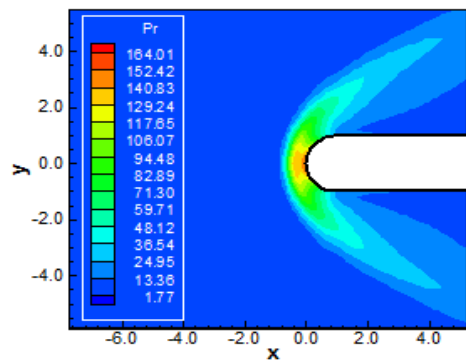
Figure 16: Pressure contours (P-C97)
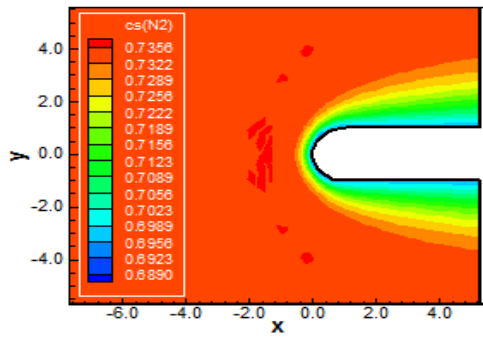
Figure 17: N₂ mass fraction contours (DK-C97)
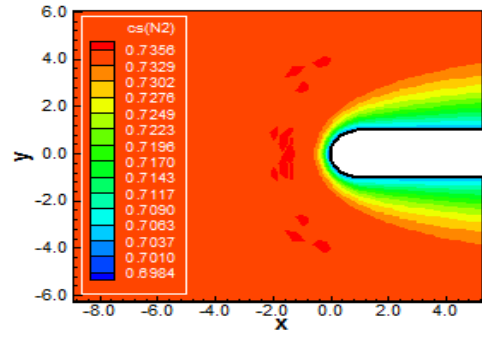
Figure 18: N₂ mass fraction contours (P-C97)
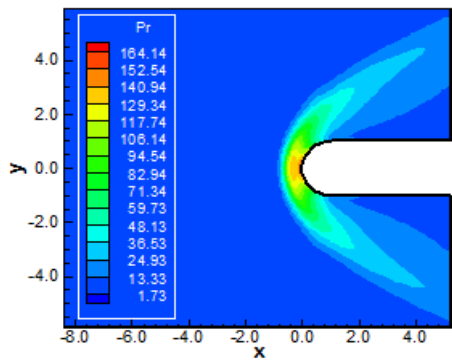
Figure 19: Pressure contours (DK-RGYB98)
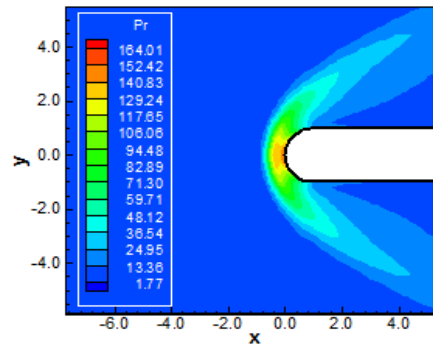
Figure 20: Pressure contours (P-RGYB98)
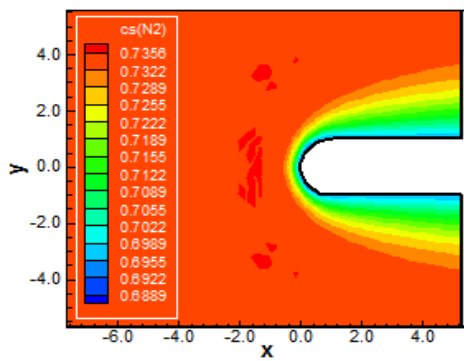
Figure 21: N₂ mass fraction contours (DK-RGYB98)
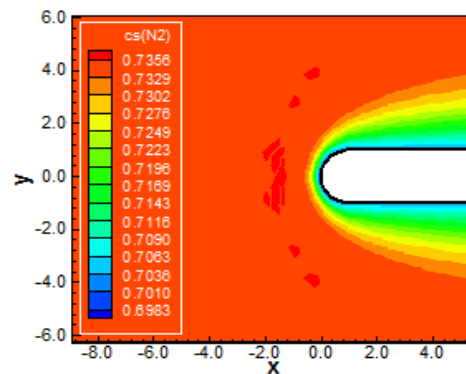
Figure 22: N₂ mass fraction contours (P-RGYB98)

Middle Point Solutions
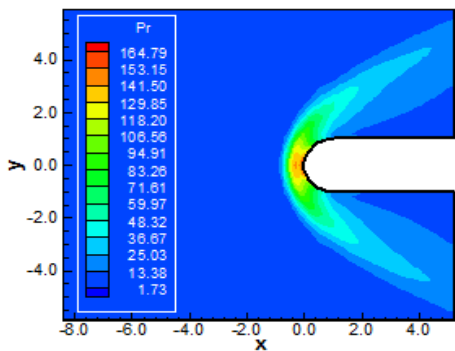
Figure 23: Pressure contours (DK-C83)
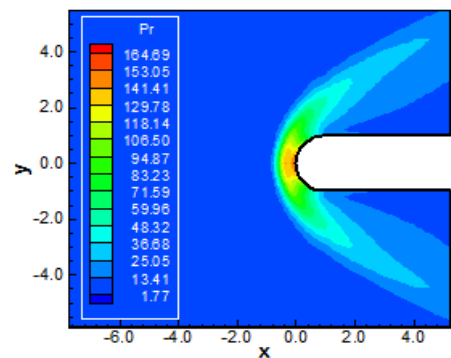
Figure 24: Pressure contours (P-C83)
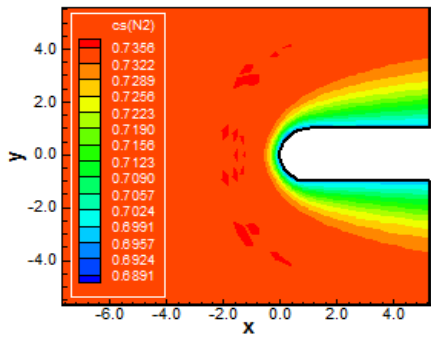
Figure 25: N$_2$ mass fraction contours (DK-C83)
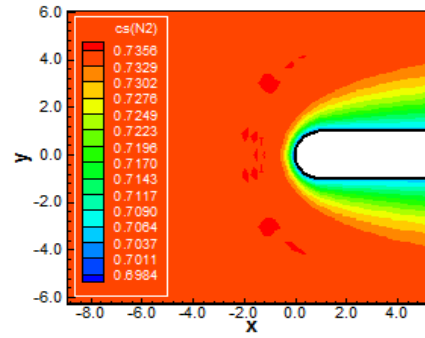
Figure 26: N$_2$ mass fraction contours (P-C83)
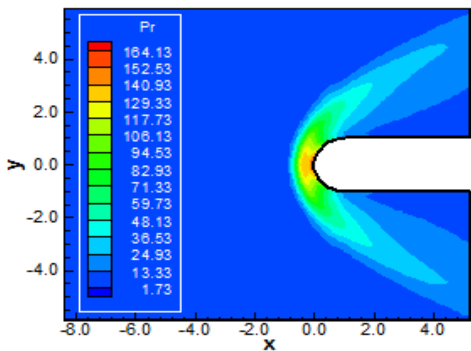
Figure 27: Pressure contours (DK-W88)
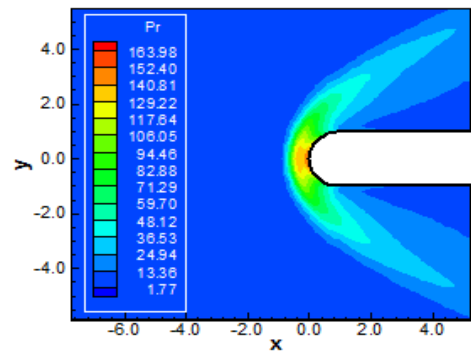
Figure 28: Pressure contours (P-W88)
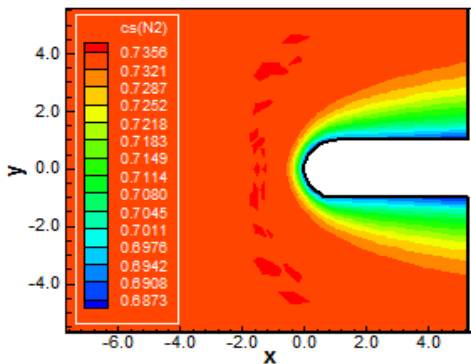
Figure 29: N$_2$ mass fraction contours (DK-W88)
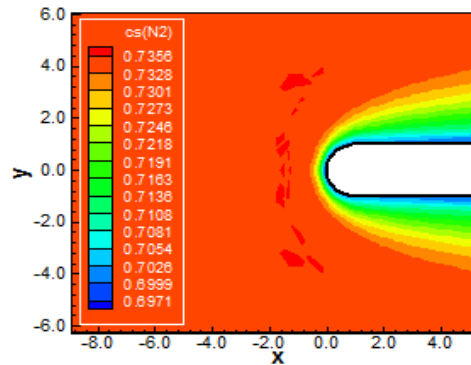
Figure 30: N$_2$ mass fraction contours (P-W88)
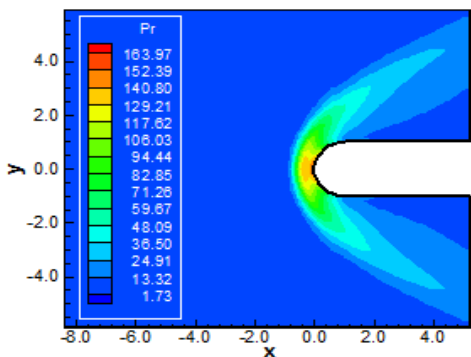
Figure 31: Pressure contours (DK-YGO96)
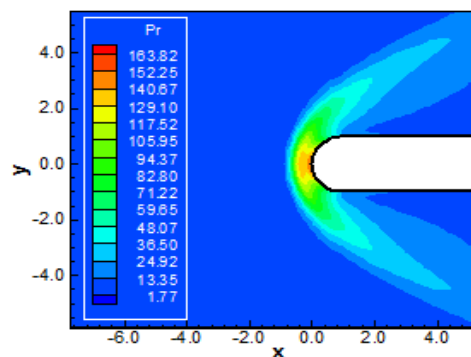
Figure 32: Pressure contours (P-YGO96)

Journal of Scientific and Engineering Research
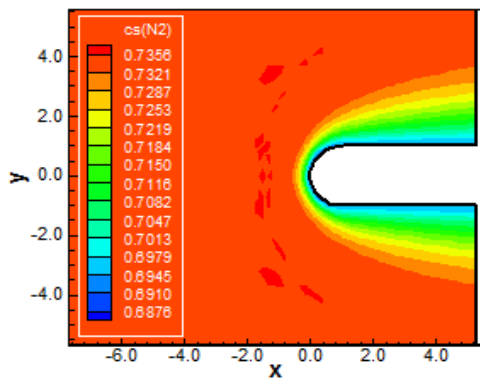
Figure 33: N₂ mass fraction contours (DK-YGO96)
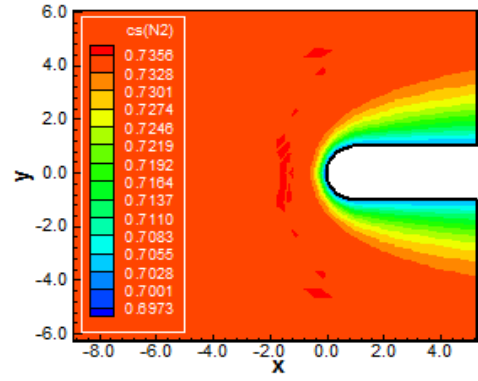
Figure 34: N₂ mass fraction contours (P-YGO96)
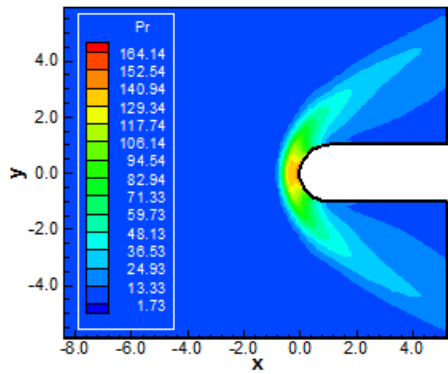
Figure 35: Pressure contours (DK-C97)
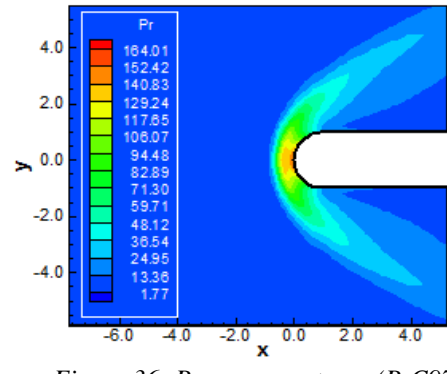
Figure 36: Pressure contours (P-C97)
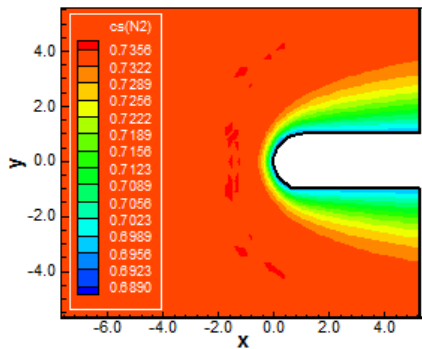
Figure 37: N₂ mass fraction contours (DK-C97)
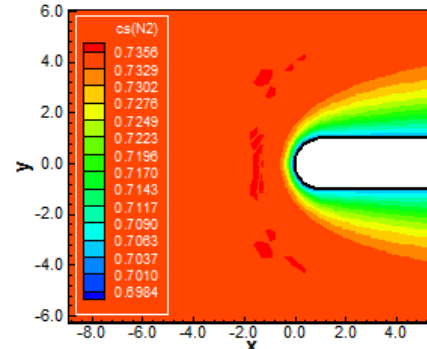
Figure 38: N₂ mass fraction contours (P-C97)
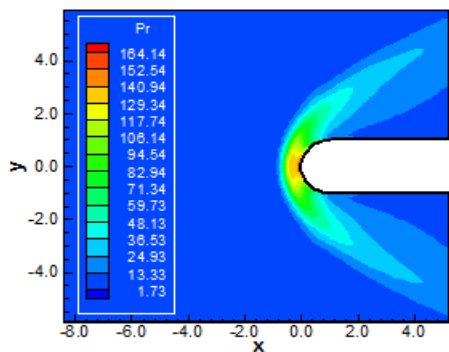
Figure 39: Pressure contours (DK-RGYB98)
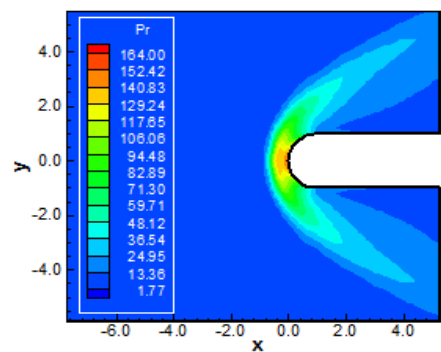
Figure 40: Pressure contours (P-RGYB98)
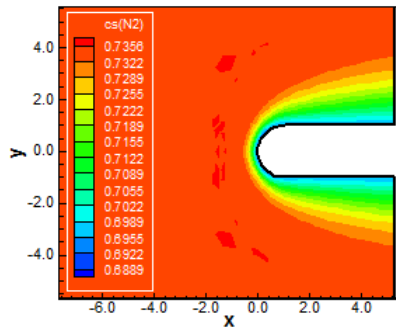
Figure 41: N₂ mass fraction contours (DK-RGYB98)
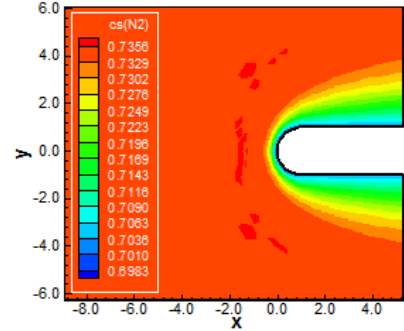
Figure 42: N₂ mass fraction contours (P-RGYB98)

Runge-Kutta 4ᵗʰ Solutions
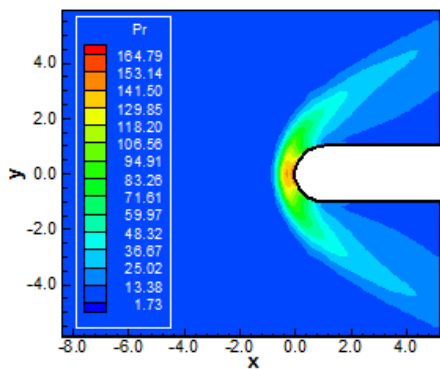
Figure 43: Pressure contours (DK-C83)
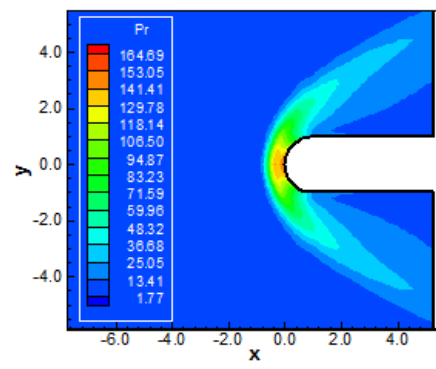
Figure 44: Pressure contours (P-C83)
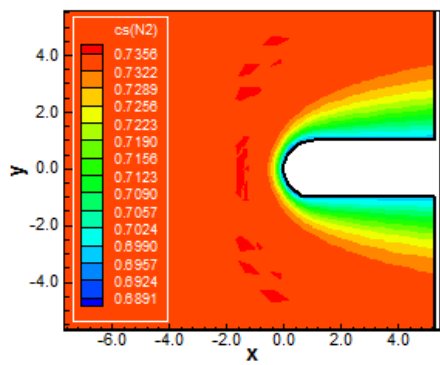
Figure 45: N₂ mass fraction contours (DK-C83)
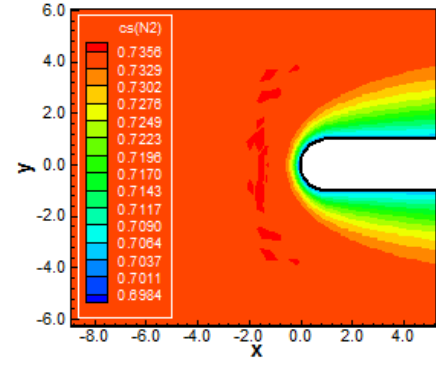
Figure 46: N₂ mass fraction contours (P-C83)
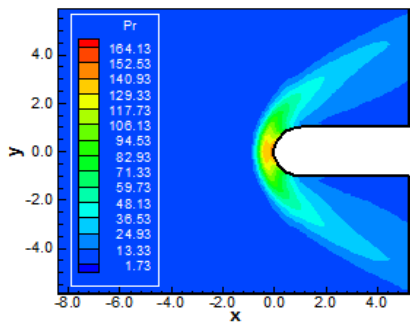
Figure 47: Pressure contours (DK-W88)
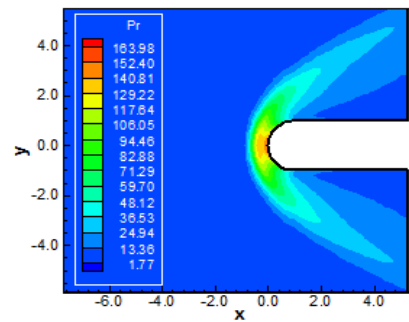
Figure 48: Pressure contours (P-W88)
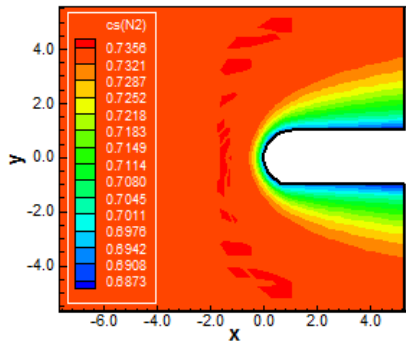
Figure 49: N₂ mass fraction contours (DK-W88)
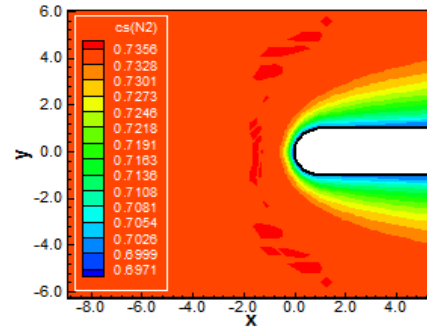
Figure 50: N₂ mass fraction contours (P-W88)
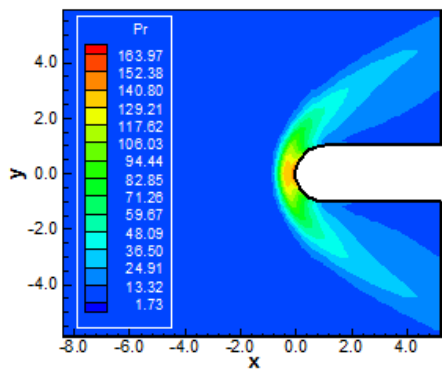
Figure 51: Pressure contours (DK-YGO96)
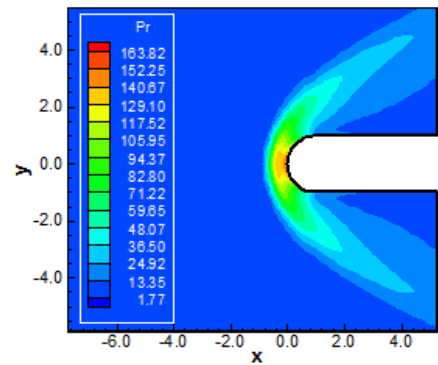
Figure 52: Pressure contours (P-YGO96)
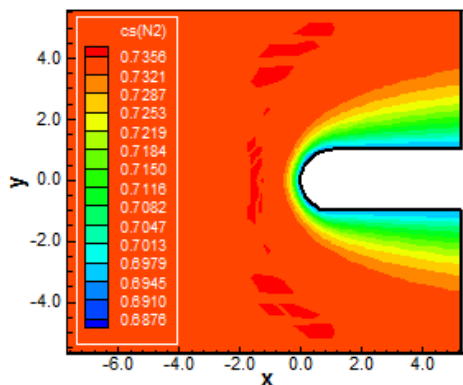
Figure 53: N₂ mass fraction contours (DK-YGO96)
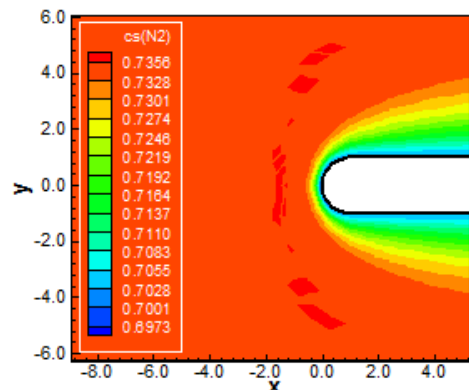
Figure 54: N₂ mass fraction contours (P-YGO96)
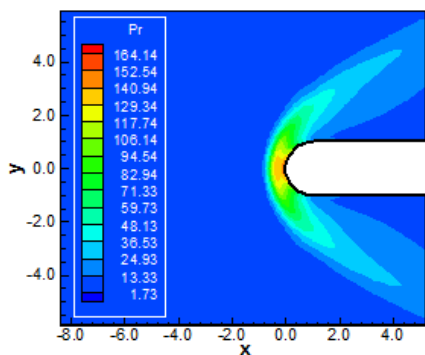
Figure 55:Pressure contours (DK-C97)
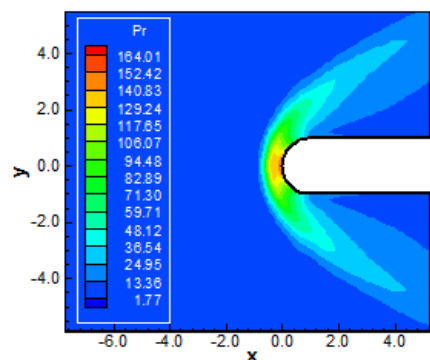
Figure 56: Pressure contours (P-C97)
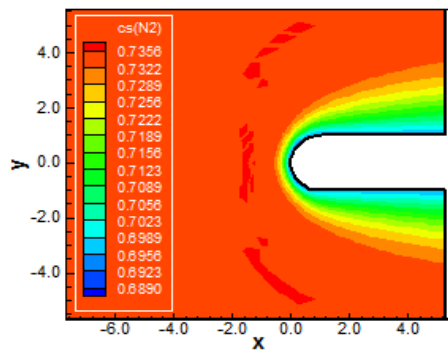
Figure 57: N_2 mass fraction contours (DK-C97)
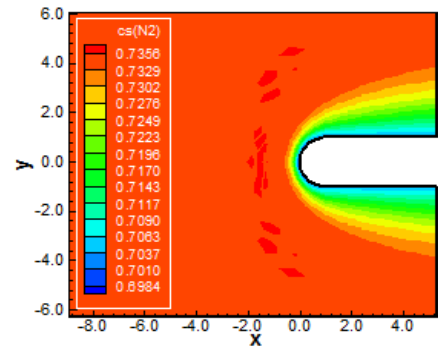
Figure 58: N_2 mass fraction contours (P-C97)
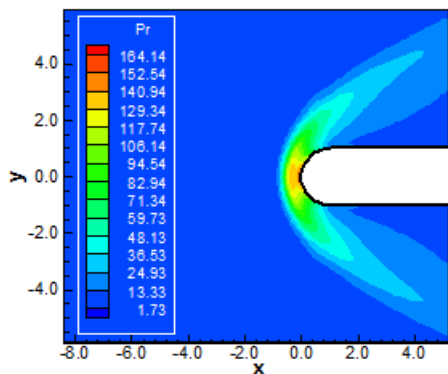
Figure 59: Pressure contours (DK-RGYB98)
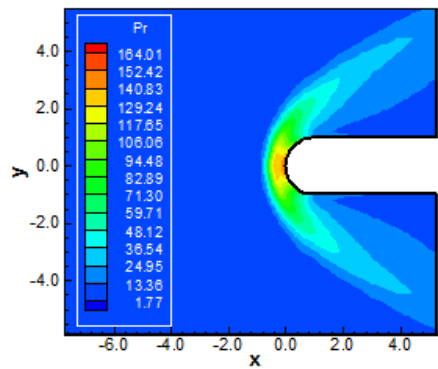
Figure 60: Pressure contours (P-RGYB98)
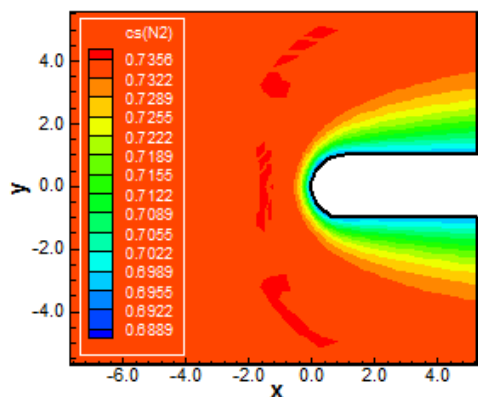
Figure 61: N_2 mass fraction contours (DK-RGYB98)
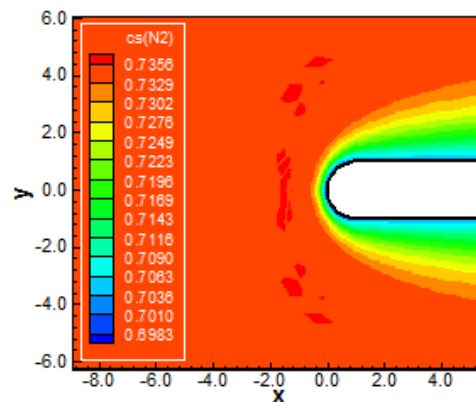
Figure 62: N_2 mass fraction contours (P-RGYB98).

12. Conclusions

In this work, a study involving magnetic field actuation over turbulent reentry flows in thermochemical non-equilibrium condition was performed. The Favre averaged Navier-Stokes equations coupled with the Maxwell equations, in conservative and finite volume contexts, employing structured spatial discretization, were studied. The numerical algorithm of Maciel was used to perform the reentry flow numerical experiments, which gave us an original contribution to the CFD community. Two types of numerical dissipation models were applied, namely: [46-47]. The "hot gas" hypersonic flow around a blunt body, in two-dimensions, was simulated. The convergence process was accelerated to steady state condition through a spatially variable time step procedure, which had proved effective gains in terms of computational acceleration [27-28]. Three time integration methods were tested to march the scheme in time, and it was another relevant contribution to the present work.

They were: Euler Backward, Middle Point, and Runge-Kutta 4th order. The reactive simulations involved Earth atmosphere chemical model of eleven species and thirty-two reactions, based on the [29] model, and forty-three reactions, based on the [30] model. The work of [25, 26] was the reference one to present the fluid dynamics and Maxwell equations of electromagnetism based on a conservative and finite volume formalisms.

The results have indicated that the Maciel scheme, with the [46] artificial dissipation operator, using the [29] chemical model coupled with the [13] turbulence model yielded the best prediction of the stagnation pressure value. Moreover, the lift coefficient was again better predicted by the Maciel scheme, with the [46] artificial dissipation operator, employing the [29] chemical model coupled with the [13] turbulence model. This work is the couple of the [26] study, involving perfect gas magnetic actuation, [34-35] studies, involving reactive reentry flows, and [52-53], related to turbulent reactive flows, in two-dimensions.

It is important to emphasize the result above where errors inferior to 5.00% were obtained for the estimation of the stagnation pressure. In the [43] work, similar studies were performed for a seven species chemical model, considering the five turbulence models studied herein and the same magnetic formulation. Errors close to 10.00% were found. Comparing these studies, it is evident that an eleven species chemical model was more realistic and represents better the flow field. With errors inferior to 5.00%, the present formulation is better than the seven species chemical model studied in [43] and is recommended as providing better treatment of the hypersonic flow under study.

References

[1].   Narayan JR, Girimaji SS. Turbulent reacting flow computations including turbulence-chemistry interactions. AIAA Paper 92-0342; 1992.

[2].   Gnoffo PA, Gupta RN, Shinn JL. Conservation equations and physical models for hypersonic flows in thermal and chemical nonequilibrium. NASA TP 2867; 1989.

[3].   Liu M, Vinokur M. Upwind algorithms for general thermo-chemical nonequilibrium flows. AIAA Paper 89-0201; 1989.

[4].   Park C. Radiation enhancement by nonequilibrium in Earth's atmosphere. Journal of Spacecraft and Rockets, 1985; 22(1): 27-36.

[5].   Park C. Problem of rate chemistry in the flight regimes of aeroassissted orbital transfer vehicles. Thermal design of aeroassissted orbital transfer vehicles. Progress in Astronautics and Aeronautics. Edited by H. F. Nelson, AIAA, NY, 1985; 96: 511-537.

[6].   Gnoffo PA. Three-dimensional AOTV flow fields in chemical nonequilibrium. AIAA Paper 86-0230; 1986.

[7].   Li CP. Implicit methods for computing chemically reacting flow. NASA TM-58274; 1986.

[8].   Lee JH. Basic governing equations for the flight regimes of aeroassisted orbital transfer vehicles. Thermal design of aeroassisted transfer vehicles. Progress in Astronautics and Aeronautics, AIAA, 1985; 96: 3-53.

[9].   Park C. Convergence of computation of chemically reacting flows. Thermophysical aspects of reentry flows. Progress in Astronautics and Aeronautics. Edited by J. N. Moss and C. D. Scott, AIAA, NY, 1986; 103: 478-513.

[10].   Park C. Assessment of two-temperature kinetic model for dissociating and weakly-ionizing Nitrogen. AIAA Paper 86-1347; 1986.

[11].   Park C. Calculation of nonequilibrium radiation in the flight regimes of aeroassissted orbital transfer vehicles. Thermal design of aeroassissted orbital transfer vehicles. Progress in Astronautics and Aeronautics. Edited by H. F. Nelson, AIAA, NY, 1985; 96: 395-418.

[12].   Park C. Nonequilibrium air radiation (NEQAIR) program: User's manual. NASA TM-86707; 1985.

[13].   Coakley TJ. Turbulence modeling methods for the compressible Navier-Stokes equations. AIAA Paper 83-1693; 1983.

[14].   Wilcox DC. Reassessment of the scale-determining equation for advanced turbulence models. AIAA Journal, 1988; 26(11): 1299-1310.

[15]. Yoder DA, Georgiadids NJ, Orkwis PD. Implementation of a two-equation k-omega turbulence model in NPARC. AIAA Paper 96-0383; 1996.

[16]. Coakley TJ. Development of turbulence models for aerodynamic applications. AIAA Paper 97-2009; 1997.

[17]. Rumsey CL, Gatski TB, Ying SX, Bertelrud A. Prediction of high-lift flows using turbulent closure models. AIAA Journal, 1998; 36(5): 765-774.

[18]. Davidson PA. Magnetohydrodynamics in materials processing. Ann. Rev. Fluid Mech., 1999; 31: 273-300.

[19]. Ziemer RW, Bush WB. Magnetic field effects on bow shock stand-off distance. Physical Review Letters, 1958; 1(2): 58-59.

[20]. Meyer RX. Magnetohydrodynamics and aerodynamic heating. ARS Journal, 1959; 29(3): 187-192.

[21]. Gurijanov EP, Harsha PT. AJAX: New directions in hypersonic technology. AIAA Paper 96-4609; 1996.

[22]. Brichkin DI, Kuranov AL, Sheikin EG. MHD-technology for scramjet control. AIAA Paper 98-1642; 1998.

[23]. Ganiev YC, Gordeev VP, Krasilnikov AV, Lagutin VI, Otmennikov VN, Panasenko AV. Theoretical and experimental study of the possibility of reducing aerodynamic drag by employing plasma injection. AIAA Paper 99-0603; 1999.

[24]. Adamovich IV, Subramanian VV, Rich JW, Macheret SO. Phenomenological analysis of shock-wave propagation in weakly ionized plasmas. AIAA Journal, 1998; 36(5): 816-822.

[25]. Gaitonde DV. Development of a solver for 3-D non-ideal magnetogasdynamics. AIAA Paper 99-3610; 1999.

[26]. Maciel ESG. Magnetic formulation and first-order schemes in 2D and 3D – Euler, Navier-Stokes and Maxwell equations in 2D and 3D – Perfect gas formulation. Saarbrücken, Deutschland: Lambert Academic Publishing (LAP), 2015; Ch. 7: 225-290.

[27]. Maciel ESG. Simulations in 2D and 3D applying unstructured algorithms, Euler and Navier-Stokes equations – Perfect gas formulation. Saarbrücken, Deutschland: Lambert Academic Publishing (LAP), 2015; Ch. 1: 26-47.

[28]. Maciel ESG. Simulations in 2D and 3D applying unstructured algorithms, Euler and Navier-Stokes equations – Perfect gas formulation. Saarbrücken, Deutschland: Lambert Academic Publishing (LAP), 2015; Ch. 6: 160-181.

[29]. Dunn MG, Kang SW. Theoretical and experimental studies of reentry plasmas. NASA CR-2232; 1973.

[30]. Park C. Assessment of two-temperature kinetic model for ionizing air. Journal of Thermophysics and Heat Transfer, 1989; 3(13): 233-244.

[31]. Narayan JR. Computation of compressible reacting flows using a two-equation turbulence model, Proceedings of the 4th International Symposium on Computational Fluid Dynamics, Davis, California, September, 1991.

[32]. Williams FA. Combustion theory. Addison-Wesley Publishing Company, Inc., Reading, MA, 1965.

[33]. Drummond JP, Carpenter MH, Riggins DW. Mixing and mixing enhancement in supersonic reacting flows. High speed propulsion systems: Contributions to thermodynamic analysis. Ed. E. T. Curran and S. N. B. Murthy, American Institute of Astronautics and Aeronautics (AIAA), Washington, D. C., 1990.

[34]. Maciel ESG. Hypersonic reactive flow simulations in two-dimensions, chemical and thermochemical non-equilibrium conditions. Saarbrücken. Deutschland: Lambert Academic Publishing (LAP), 2015; Ch. 7: 491-589.

[35]. Maciel ESG. Hypersonic reactive flow simulations in two-dimensions, chemical and thermochemical non-equilibrium conditions. Saarbrücken. Deutschland: Lambert Academic Publishing (LAP), 2015; Ch. 8: 590-687.

[36]. Favre A. Statistical equations of turbulent gases. Institut de Mechanique Statistique de la Turbulence, Marseille.

[37]. Harlow FH, Nakayama PI. Turbulence transport equations. The Physics of Fluids, 1967; 10(11): 2323-2332.

[38]. Hanjalic K, Launder BE. A Reynolds stress model of turbulence and its application to thin shear flows. J. Fluid Mech., Part 4, 1972; 52: 609-638.

[39]. Girimaji SS. A simple recipe for modeling reaction-rates in flows with turbulent combustion. AIAA Paper 91-1792; 1991.

[40]. Prabhu RK. An implementation of a chemical and thermal nonequilibrium flow solver on unstructured meshes and application to blunt bodies. NASA CR-194967; 1994.

[41]. Saxena SK, Nair MT. An improved Roe scheme for real gas flow. AIAA Paper 2005-0587; 2005.

[42]. Maciel ESG, Andrade CR. Turbulent chemical non-equilibrium reentry flows in 2D - Five species. Asian Journal of Mathematics and Computer Research, 2017; 20(3): 130-168.

[43]. Maciel ESG, Andrade CR. Turbulent thermochemical non-equilibrium reentry flows with magnetic actuation in 2D – Seven species. Asian Journal of Physical and Chemical Sciences, 2017; 3(4): 1-36.

[44]. Ait-Ali-Yahia D, Habashi WG. Finite element adaptive method for hypersonic thermochemical nonequilibriumflows. AIAA Journal, 1997; 35(8): 1294-1302.

[45]. Long LN, Khan MMS, Sharp HT. Massively parallel three-dimensional Euler / Navier-Stokes method. AIAA Journal, 1991; 29(5): 657-666.

[46]. Mavriplis DJ. Accurate multigrid solution of the Euler equations on unstructured and adaptive meshes. AIAA Journal, 1990; 28(2): 213-221.

[47]. Turkel E, Vatsa VN. Effect of artificial viscosity on three-dimensional flow solutions. AIAA Journal, 1994; 32(1): 39-45.

[48]. Vincente WG, Kruger Jr. CH. Introduction to physical gas dynamics. Malabar, Florida, EUA: Krieger Publishing Company, 2002; Ch. 1: 1-26.

[49]. Fox RW, McDonald AT. Introdução à mecânica dos fluidos. Guanabara Editor, 1988.

[50]. Maciel ESG. Simulação numérica de escoamentos supersônicos e hipersônicos utilizando técnicas de dinâmica dos fluidos computacional. Doctoral thesis. ITA, CTA, São José dos Campos, SP, Brazil, 2002.

[51]. Anderson Jr. JD. Fundamentals of aerodynamics, McGraw-Hill, Inc., 5th Edition, 2010.

[52]. Maciel ESG. Turbulent thermochemical non-equilibrium reentry flows in 2D. Computational and Applied Mathematics Journal, 2015; 1(4): 201-224.

[53]. Maciel ESG, Andrade CR. Turbulent thermochemical non-equilibrium reentry flows in 2D - Eleven species. Asian Journal of Mathematics and Computer Research, 2017; 20(4): 179-217.